

# From strong to weak correlations in breathing-mode kagome van der Waals materials: $\text{Nb}_3(\text{F},\text{Cl},\text{Br},\text{I})_8$ as a robust and versatile platform for many-body engineering

Joost Aretz,<sup>1</sup> Sergii Grytsiuk,<sup>1</sup> Xiaojing Liu,<sup>2</sup> Giovanna Feraco,<sup>2</sup> Chrystalla Knekna,<sup>2,3</sup> Muhammad Waseem,<sup>2</sup> Zhiying Dan,<sup>2</sup> Marco Bianchi,<sup>4</sup> Philip Hofmann,<sup>4</sup> Mazhar N. Ali,<sup>5</sup> Mikhail I. Katsnelson,<sup>1</sup> Antonija Grubišić-Čabo,<sup>2</sup> Hugo U. R. Strand,<sup>6</sup> Erik G. C. P. van Loon,<sup>7</sup> and Malte Rösner<sup>1,\*</sup>

<sup>1</sup>*Institute for Molecules and Materials, Radboud University, Heijendaalseweg 135, 6525AJ Nijmegen, The Netherlands*

<sup>2</sup>*Zernike Institute for Advanced Materials, University of Groningen, 9747 AG Groningen, The Netherlands*

<sup>3</sup>*Van der Waals-Zeeman Institute, Institute of Physics, University of Amsterdam, Science Park 904, 1098 XH, Amsterdam, The Netherlands*

<sup>4</sup>*Department of Physics and Astronomy, Interdisciplinary Nanoscience Center (iNANO), Aarhus University, 8000 Aarhus C, Denmark*

<sup>5</sup>*Kavli Institute of Nanoscience, Delft University of Technology, Lorentzweg 1, 2628 CJ Delft, the Netherlands*

<sup>6</sup>*School of Science and Technology, Örebro University, SE-701 82 Örebro, Sweden*

<sup>7</sup>*NanoLund and Division of Mathematical Physics, Department of Physics, Lund University, Lund, Sweden*

By combining ab initio downfolding with cluster dynamical mean-field theory, we study the degree of correlations in the low-temperature structures of the breathing-mode kagome van der Waals materials  $\text{Nb}_3(\text{F},\text{Cl},\text{Br},\text{I})_8$ . We show that the Coulomb correlation strength steadily increases from I to Br, Cl, and F, allowing us to identify  $\text{Nb}_3\text{I}_8$  as a weakly correlated (obstructed atomic) insulator whose gap is only mildly affected by the local Coulomb interaction.  $\text{Nb}_3\text{Br}_8$  and  $\text{Nb}_3\text{Cl}_8$  are strongly correlated insulators, whose gaps are significantly influenced by Coulomb-induced vertex corrections.  $\text{Nb}_3\text{F}_8$  is a prototypical bulk Mott-insulator whose gap is initially opened by strong correlation effects. Angle-resolved photoemission spectroscopy measurements comparing  $\text{Nb}_3\text{Br}_8$  and  $\text{Nb}_3\text{I}_8$  allow us to experimentally confirm these findings by revealing spectroscopic footprints of the degree of correlation. Our calculations further predict that the entire material family can be tuned into correlated charge-transfer or Mott-insulating phases upon electron or hole doping. Our magnetic property analysis additionally shows that inter-layer magnetic frustrations in the high-temperature phase drive the lattice phase transition to the low-temperature structures. The accompanying bilayer hybridization through inter-layer dimerization yields magnetic singlet ground states in the Cl, Br, and I compounds. Our findings establish  $\text{Nb}_3\text{X}_8$  as a robust, versatile, and tunable class for van der Waals-based Coulomb and Mott engineering and allow us to speculate on the symmetry-breaking effects necessary for the recently observed Josephson diode effect in  $\text{NbSe}_2/\text{Nb}_3\text{Br}_8/\text{NbSe}_2$  heterostructures.

## I. INTRODUCTION

Correlation effects resulting from electron-electron (Coulomb) interactions are omnipresent in solids. Depending on the relative Coulomb interaction strength, they manifest in various ways, from renormalization of quasiparticle dispersions in the case of weak correlations [1], via induced shake-off/replica bands in the case of intermediate correlations [2, 3], to completely different ground states in the case of strong correlations [4, 5]. Being able to tune the degree of correlations would therefore allow to engineer many-body properties of quantum materials [6].

The layered structure of van der Waals (vdW) materials makes them uniquely tunable [7], with opportunities such as field-effect-doping [8, 9], substrate engineering [10], heterostructuring [7], and moiré engineering [11], but also via chemical modifications [6]. Furthermore, within the library of layered vdW materials, we

now have access to a variety of correlated ground states including magnetism [12], charge-density wave (CDW) order [13], superconductivity [14, 15], as well as Mott-insulators [11, 16, 17]. However, the complex electronic structure of the systems in question and the inherent complexity and partial fragility of correlated electron physics make it challenging to fully understand the microscopic origin of the observed phenomena, let alone making predictive simulations. Thus, simple and robust correlated layered material systems with varying and tunable degrees of correlation strengths are highly desirable.

Here, we show that the transition metal halide family  $\text{Nb}_3\text{X}_8$  holds up to this promise. In their low-temperature phases, these so-called breathing-mode kagome vdW materials [18] host only two bands close to the Fermi level, which are cleanly separated from the rest of the electronic structure as a result of simultaneous in-plane trimerization of the transition metal atoms and out-of-plane dimerization of the vdW layers. Using ab initio downfolding to molecular orbitals, we derive material-specific minimal models, including single-particle (hopping) and many-body (Coulomb) interactions for the entire family  $\text{Nb}_3\text{X}_8$ , with  $\text{X} \in \{\text{F}, \text{Cl}, \text{Br}, \text{I}\}$ .

\* m.roesner@science.ru.nl

Studying them using cluster dynamical mean-field theory [19] shows how the balance between kinetic and Coulomb energy changes from  $\text{Nb}_3\text{F}_8^*$  to  $\text{Nb}_3\text{I}_8$ . In this way, we prove that  $\text{Nb}_3\text{X}_8$  realizes several correlated phases ranging from weakly correlated (obstructed atomic) insulators to strongly correlated Mott insulators, which are furthermore tunable by doping as well as by adjusting the number of involved layers as summarized in Table I.

TABLE I. Electronic phases of bulk and monolayer  $\text{Nb}_3\text{X}_8$  for different doping levels.  $N_e$  labels the number of electrons in the low-energy subspace. For bulk (monolayer)  $N_e = 2$  ( $N_e = 1$ ) labels the undoped case.  $\delta$  refers to small doping with  $0 < \delta \lesssim 0.5$ . The  $\text{Nb}_3\text{F}_8^*$  notations refers to its putative structure (see section II A. )

	$\text{Nb}_3\text{F}_8^*$	$\text{Nb}_3\text{Cl}_8$	$\text{Nb}_3\text{Br}_8$	$\text{Nb}_3\text{I}_8$
$N_e$	<b>Bulk (low temperature)</b>			
2	2-band Mott insulator	strongly correlated insulators		weakly correlated insulator
$2 + \delta$	correlated metals			metal
3	charge-transfer insulators		Mott insulators	
	<b>Monolayer</b>			
1	1-band Mott insulators			
$1 + \delta$	correlated metals			

### $\text{Nb}_3\text{X}_8$ Overview

$\text{Nb}_3\text{X}_8$  belongs to the class of layered vdW kagome materials, which are intensively studied due to the interplay of their non-trivial topology and intriguing correlation phenomena [18, 20].  $\text{Nb}_3\text{X}_8$  specifically belongs to the sub-class of breathing-mode kagome materials, with alternating in-plane bond lengths, as illustrated in Fig. 1. Among them,  $\text{Nb}_3\text{Cl}_8$  and  $\text{Nb}_3\text{Br}_8$  have recently gained much attention due to their promises to represent prototypical single-band or few-band Mott insulators [21–24], possibly accompanied by strongly correlated magnetic ground states [23, 25, 26].  $\text{Nb}_3\text{Br}_8$  has received further attention due to its role in inducing field-free Josephson diode effects in  $\text{NbSe}_2/\text{Nb}_3\text{Br}_8/\text{NbSe}_2$  heterostructures [27]. Although some scenarios have been suggested [28], it is not yet clear what microscopic behavior yields the required symmetry breakings and whether it is intrinsic to  $\text{Nb}_3\text{Br}_8$  or related to the interfaces.

Experimentally, X-ray diffraction shows a lattice phase transitions in  $\text{Nb}_3\text{Cl}_8$  and  $\text{Nb}_3\text{Br}_8$  from high- to low-temperature structures, which can be understood as a shift in the vdW layer stacking [29, 30]. Raman spectroscopy [31] corroborates this interpretation but also indicates that phonon symmetries are not affected by the

transition. Angle-resolved photoemission spectroscopy (ARPES) data shows gapped electronic structures with rather flat, albeit broadened, bands below the Fermi level for bulk  $\text{Nb}_3\text{I}_8$  [32],  $\text{Nb}_3\text{Cl}_8$  [33] and  $\text{Nb}_3\text{Br}_8$  [24, 34] as well as their admixtures [22]. For  $\text{Nb}_3\text{Cl}_{8-x}\text{Br}_x$ , the magnetic susceptibility further shows a Curie-Weiss behavior at elevated temperatures in the high-temperature phases, accompanied by a sudden drop upon entering the low-temperature phase [22, 25, 29, 30, 33, 35]. This has been interpreted as a transition from a paramagnetic to a non-magnetic phase, and the finite susceptibility at very low temperatures is ascribed to magnetic impurities [29, 30].

Theoretically, the modeling of these materials takes place in several steps. A first impression is given by Density Functional Theory (DFT), which has been used to study the monolayer, bilayer, and bulk structures, in both low- and high-temperature crystal structures [21, 23, 32, 36, 37]. Starting with the monolayer, DFT shows a single, rather flat band crossing the Fermi level, which is half-filled and thus hosts exactly one electron per unit cell. At low temperatures and going to bilayer and bulk structures, there is an alternating strong and weak hybridization between adjacent layers, which leads to a dimerization in the out-of-plane direction [21–24]. In this case, DFT predicts two rather flat bands around the Fermi level, which show a small, but finite hybridization gap. Since flat bands are indicators for low kinetic energies, the role of competing Coulomb interactions needs to be carefully taken into account. Mean-field DFT calculations are, however, known to underestimate the impact of the latter, especially in the case of  $d$  orbitals, which dominate the low-energy space in the case of  $\text{Nb}_3\text{X}_8$ . Therefore, beyond mean-field theories, which take possibly strong Coulomb interactions accurately into account, are necessary. In the context of  $\text{Nb}_3\text{X}_8$ , so far this has been done only in the case of monolayer  $\text{Nb}_3\text{Cl}_8$  [22, 23, 38], generic bilayer models for  $\text{Nb}_3\text{Cl}_8$  and  $\text{Nb}_3\text{Br}_8$  [21], as well as simplified models of bulk  $\text{Nb}_3\text{Cl}_8$  [23] and  $\text{Nb}_3\text{Br}_8$  [24] using higher-level many-body theory, such as dynamical mean-field theory, or alternative supercell approaches [39]. All of these calculations hint towards an intriguing interplay between enhanced Coulomb interactions and kinetic energies, which seem to drive variants of Mott insulating states. For bulk structures, this especially requires a careful analysis of the impact of the out-of-plane dimerization, which has so far only been discussed qualitatively for bilayers of  $\text{Nb}_3\text{Br}_8$  and  $\text{Nb}_3\text{Cl}_8$  [21] as well as for bulk  $\text{Nb}_3\text{Br}_8$  [24].

## II. RESULTS

To systematically, material-specifically, and quantitatively study these effects, we calculate and investigate all kinetic and Coulomb interaction terms in the low-temperature structures of  $\text{Nb}_3\text{X}_8$  with  $\text{X} \in \{\text{F}, \text{Cl}, \text{Br}, \text{I}\}$  and solve the resulting models using cluster dynamical

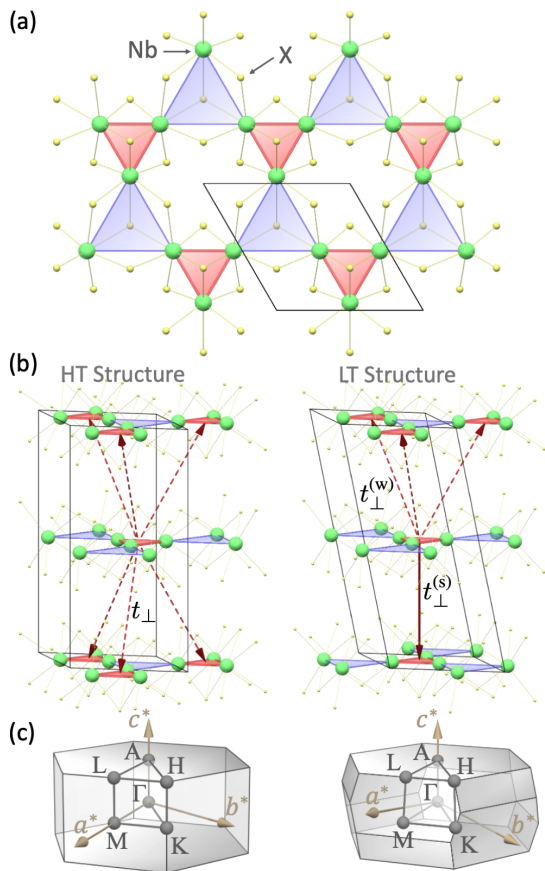


FIG. 1.  **$\text{Nb}_3\text{X}_8$  Crystal Structures.** (a) single layer (top view) and (b) bulk structures (side view) at high and low temperatures, respectively. Darker red solid (dashed) arrows indicate strong (weak) interlayer couplings  $t_{\perp}^s$  ( $t_{\perp}^w$ ) between the nearest trimers. The gray lines in (a) and (b) represent the primitive unit cell. (c) illustrates the Brillouin zones and high-symmetry points for both structures.

mean-field theory.

### A. $\text{Nb}_3\text{X}_8$ Crystal Structure

The breathing-mode kagome structure depicted in Fig. 1 (a) yields an in-plane trimerization of Nb atoms (see small triangles in red). In the out-of-plane direction, there exist two stackings, referred to as the high-temperature (HT) and low-temperature (LT) structures, which are depicted in Fig. 1 (b) together with their Brillouin zones in Fig. 1 (c). The LT stacking leads to a dimerization in the out-of-plane direction with alternating strong and weak hybridization between adjacent layers, as indicated by dashed and solid line arrows in Fig. 1 (b) and discussed in more detail below.  $\text{Nb}_3\text{Cl}_8$  and  $\text{Nb}_3\text{Br}_8$  undergo a structural phase transition that changes the stacking from the HT to the LT structures at 90 K and 382 K, respectively [29, 30, 35, 40]. While it is hypothesized that  $\text{Nb}_3\text{I}_8$  exhibits a similar transition at even higher temperatures,

this has yet to be confirmed experimentally.

At high temperatures, crystals of both  $\text{Nb}_3\text{Cl}_8$  and  $\text{Nb}_3\text{Br}_8$  belong to the  $\text{P}\bar{3}m1$  space group. However, at low temperatures,  $\text{Nb}_3\text{Br}_8$  and  $\text{Nb}_3\text{I}_8$  have been reported to adopt the  $\text{R}\bar{3}m$  space group [35, 40]. In contrast, the crystal structure of  $\text{Nb}_3\text{Cl}_8$  has been described inconsistently in different studies, with reported space groups of  $\text{R}\bar{3}$  [30],  $\text{R}\bar{3}m$  [31, 35, 40], and  $\text{C}2/m$  [29]. Since the  $\text{R}\bar{3}m$  structures have not been reported in detail, while the  $\text{R}\bar{3}$  structure has, we will use the latter for  $\text{Nb}_3\text{Cl}_8$  in the following discussion. We note that this symmetry reduction has minimal impact on the correlation effects and electronic structure as demonstrated in Ref. [23].

To the best of our knowledge, only Cl, Br, and I have been synthesized, but the addition of  $\text{Nb}_3\text{F}_8^*$  gives a unified view of the full series. To emphasize that  $\text{Nb}_3\text{F}_8^*$  is putative, we will use the starred notation. To construct the LT  $\text{Nb}_3\text{F}_8^*$  crystal structure we assume  $\text{R}\bar{3}m$  symmetry, extrapolate the lattice vectors based on the other compounds, and perform a structural optimization of the atomic positions (see Methods for details).

## B. Electronic Structure

### 1. Origin of Robust Flat Bands

The formation of flat bands in  $\text{Nb}_3\text{X}_8$  plays a crucial role in their electronic and magnetic properties. As the underlying lattice structure is of kagome type, it has been suspected that the flat bands originate from the topologically non-trivial flat bands of the well-known generic kagome band structure as described, e.g., by tight-binding models with isotropic hoppings; see for example Refs. 33 and 41. However, as the low energetic orbitals of all  $\text{Nb}_3\text{X}_8$  compounds are of predominant Nb  $d$  character, this simplified picture has to be reconsidered [42]. Therefore, we calculated the electronic structure of LT  $\text{Nb}_3\text{Br}_8$  at different levels of the breathing mode perturbation, which is measured by the ratio  $d_2/d_1$ , where  $d_1$  and  $d_2$  represent the sizes of the small and large triangles, respectively. When the structure is a conventional kagome lattice ( $d_1 = d_2$ ), the octahedral crystal field causes the  $d$  orbitals of the Nb ions to split into the lower-energy  $t_{2g}$  ( $d_{xy}$ ,  $d_{yz}$ , and  $d_{xz}$ ) and the higher-energy  $e_g$  ( $d_{x^2-y^2}$  and  $d_{z^2}$ ) states. In the actual breathing-mode ground state ( $d_2/d_1 \approx 1.45$ ), the octahedral crystal field is distorted, and the  $t_{2g}$  states are further split into two sublevels labeled  $t_{2g}^1$  and  $t_{2g}^2$ .

In Fig. 2 we show the corresponding DFT band structures, starting from the unperturbed conventional kagome lattice ( $d_2/d_1 = 1$ ) and indicate Nb  $t_{2g}^1$  orbitals in red, Nb  $t_{2g}^2$  orbitals in green, and Nb  $e_g$  orbitals in blue. From this, we see that in the putative conventional kagome structure,  $\text{Nb}_3\text{Br}_8$  would be a metal with various Nb  $d$  bands crossing the Fermi level. Upon introducing the breathing mode perturbation, we see that the Nb  $t_{2g}^2$  bands (start to) fully gap, while the Nb  $t_{2g}^1$  bands stay

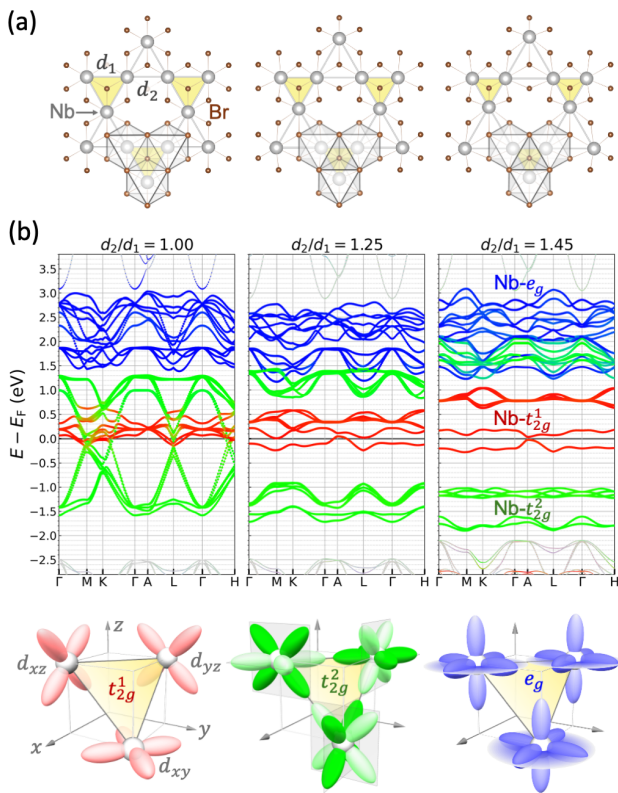


FIG. 2. **Breathing Mode-Induced Flat Band Formation in Low-Temperature  $\text{Nb}_3\text{Br}_8$ .** (a) and (b) illustrate the crystal structure (showing only one layer for clarity) and the electronic structure as a function of the size ratio of the small and large triangles  $d_2/d_1$ . The electronic structures in (b) are weighted between  $\text{Nb}-t_{2g}^1$  (in red),  $\text{Nb}-t_{2g}^2$  (in green), and  $\text{Nb}-e_g$  (in blue) states, respectively. Black lines in (a) depict the ideal (left panel) and distorted (two following panels) octahedral environment surrounding the Nb atoms.

behind, nearly pinned to the Fermi level. Finally, in the actual full breathing mode structure ( $d_2/d_1 \approx 1.45$ ), we see that the Nb  $t_{2g}^2$  bands further split into a set of two very flat bands directly around the Fermi level and a set of four unoccupied bands. Next to this, we also find that the occupied Nb  $t_{2g}^2$  bands split, yielding two sets of very flat bands, while their unoccupied counterparts only mildly change in their dispersion and now overlap in energy with the Nb  $e_g$  bands.

The flat band formation in  $\text{Nb}_3\text{X}_8$  is thus intimately connected to the Nb trimerization within the breathing mode distortion. In the monolayer limit, we already showed that the Nb  $t_{1g}$  band at the Fermi level can be best understood as being formed by a molecular orbital centered at the breathing-mode induced Nb trimer [23]. As such, the origin of the two well-separated low-energy flat bands around the Fermi level in  $\text{Nb}_3\text{X}_8$  is very similar to the formation of flat bands in the star-of-David phase of  $\text{TaS}_2$  [13] or twisted bilayer graphene (TBG) [43]: due to new, larger structures (induced by the CDW in  $\text{TaS}_2$ , the moiré potential in TBG, or here the breathing-mode

distortion), new effective orbitals are formed, which are spatially rather far apart from each other. This large spatial separation yields a small effective hopping of electrons between these new effective CDW, moiré, or here molecular orbitals, such that their resulting bands are only weakly dispersive. Simultaneously, gaps in the background electronic structures are opened, leaving (nearly) disentangled flat bands behind. All of this is lifted upon destroying the larger structure, i.e. by melting the CDW in  $\text{TaS}_2$ , tuning away from the magic angle in TBG, or suppressing the breathing mode distortion in  $\text{Nb}_3\text{X}_8$ .

The key advantage of  $\text{Nb}_3\text{X}_8$  is that its breathing mode distortion is a stable ground state (at all reported temperatures and doping levels) that does not require a precisely tuned twist angle or temperature-induced stabilization. The formation of flat bands in  $\text{Nb}_3\text{X}_8$  is thus very robust, so that resulting correlation effects can be studied without additional complications.

## 2. Molecular Orbital Basis

Having established the breathing mode distortion as the mechanism producing the disentangled flat bands, we are now ready to study the correlation trend across  $\text{Nb}_3\text{X}_8$  family. In Fig. 3, we show the bulk DFT band structures in the LT phases. As expected, we find two relatively flat bands around the Fermi level in all cases. In the case of  $\text{Nb}_3\text{F}_8^*$ , both bands cross the Fermi level, while for the others, we consistently find one fully occupied and one completely unoccupied band. For in-plane momenta ( $k_z = 0$ ), the two bands are clearly split apart, while for the out-of-plane momentum direction  $\Gamma - A$ , we observe a stronger dispersion, and the gap nearly closes. As will become clear from the subsequent Wannierization discussed below, this  $k_z$  behaviour is a result of the interlayer dimerization of trimers within the strongly hybridized bilayers. Thus, in  $k_z$ , the low-energetic electronic structure is reminiscent of the behaviour of the Su-Schrieffer-Heeger (SSH) model [44], which consequently yields a gap in this direction, due to the mismatch of the alternating out-of-plane hopping matrix elements. From Cl to Br and I, we already see the first clear trend in the material class: the in-plane gap between these two bands steadily increases.

To prepare for the downfolding and to further analyze the low-energetic band structure, we construct maximally localized Wannier functions for the two low-energy bands. In all four cases, we find that the bands can be perfectly Wannier-interpolated within a basis spanned by two molecular orbitals  $\psi_1$  and  $\psi_2$ , which are centered on trimers of adjacent layers and which are directly above each other, see Fig. 4. In this molecular orbital basis, we find similar contributions of both orbitals to both low-energy bands. However, upon diagonalization of the single-particle Wannier Hamiltonian, we find that the lower (occupied) band is well described by a bonding orbital  $\psi^{(+)}$  formed by the direct sum of the trimer-



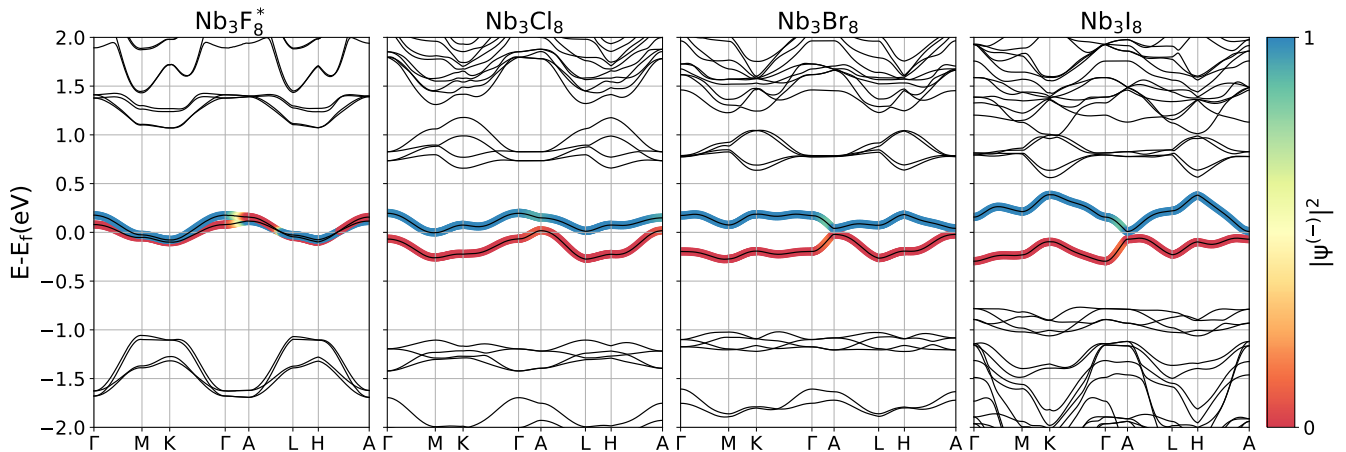


FIG. 3.  $\text{Nb}_3\text{X}_8$  DFT Bandstructures. Colors indicate the weight of the anti-bonding orbital  $|\psi^{(-)}|^2 = |\langle \psi^{(-)} | \psi \rangle|^2$ .

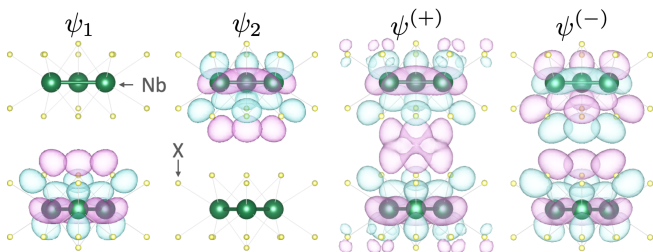


FIG. 4. Wannier Molecular Orbitals of  $\text{Nb}_3\text{Br}_8$ .  $\psi_1$  and  $\psi_2$ , along with their bonding (+) and antibonding (-) combinations,  $\psi^{(\pm)} = (\psi_1 \pm \psi_2)/\sqrt{2}$ .

centered molecular orbitals  $\psi^{(+)} = (\psi_1 + \psi_2)/\sqrt{2}$ , while the upper (unoccupied) band is well described by the corresponding anti-bonding orbital  $\psi^{(-)} = (\psi_1 - \psi_2)/\sqrt{2}$ , as illustrated in Fig. 4. For the subsequent analysis, it will be helpful to switch back and forth between the molecular orbital basis ( $\psi_i$ ) and the bonding/anti-bonding basis ( $\psi^{(\pm)}$ ).

Upon projecting the Kohn-Sham states to the  $\psi^{(\pm)}$  basis, we see that this interpretation holds especially for in-plane momenta. For out-of-plane  $k_z$  momenta, however, we observe that  $\psi^{(\pm)}$  states mix, which is a result of the small, but finite wavefunction overlap between the dimerized layers. This admixture thus verifies the SSH-like behaviour in the  $k_z$  direction. This is consistent with Ref. 45 within which  $\text{Nb}_3\text{Br}_8$  and  $\text{Nb}_3\text{I}_8$  are classified as obstructed atomic insulators [46]. Although the Cl, Br, and I compounds all share the classification as obstructed atomic insulators, the details and specifically the size of the DFT gap change from material to material, as also shown by the Wannier hopping parameters in Fig. 5 and as discussed in more detail in the following.

### C. Downfolded Many-Body Hamiltonians from Constrained Random Phase Approximation Calculations

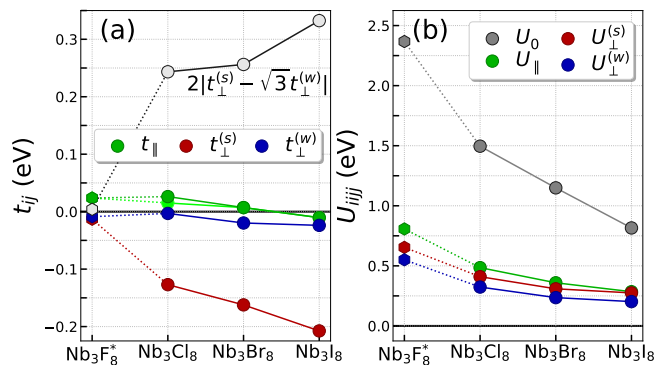


FIG. 5. Molecular Orbital Hubbard Model Parameters of  $\text{Nb}_3\text{X}_8$ . (a) In-plane  $t_{\parallel}$  and out-of-plane hopping matrix elements  $t_{\perp}^{(s)}$  and  $t_{\perp}^{(w)}$  within the molecular orbital basis. (b) cRPA Coulomb interaction matrix elements: on-site  $U_0$ , first nearest in-plane neighbors  $U_{\parallel}$ , and first and second nearest out-of-plane neighbors,  $U_{\perp}^{(s)}$ , and  $U_{\perp}^{(w)}$ , respectively, within the molecular orbital basis. The light green marker in panel (a) indicates varying in-plane hopping values for  $\text{Nb}_3\text{Cl}_8$  due to reduced symmetry.

Using the molecular orbital basis, we proceed with deriving generalized Hubbard Hamiltonians of the form

$$H = \sum_{i,j} t_{ij} c_i^\dagger c_j + \frac{1}{2} \sum_{i,j,k,l} U_{ijkl} c_i^\dagger c_j^\dagger c_k c_l \quad (1)$$

for all compounds. Here  $c_i^\dagger$  and  $c_j$  are electron creation and annihilation operators in molecular orbitals at sites  $i$  and  $j$ , respectively,  $t_{ij}$  are single-particle (hopping) and  $U_{ijkl}$  partially screened two-particle (Coulomb) matrix elements. The latter are evaluated within the constrained

random phase approximation (cRPA) [47], which accounts for all RPA-level screening processes except those taking place within the molecular orbitals  $\psi_i$ . In Fig. 5, we show a subset of these matrix elements focusing on the local and nearest-neighbor density-density Coulomb matrix elements ( $U_{ijji}$ ) as well as on intra- and inter-layer hopping matrix elements. For a complete overview, see Appendix 1.

We find that the in-plane nearest-neighbor hopping ( $t_{\parallel}$ ) is relatively small in all compounds ( $\lesssim 25$  meV in magnitude, see green markers in Fig. 5 (a), which reflects the similar rather flat in-plane (constant  $k_z$ ) dispersion with  $\text{Nb}_3\text{Br}_8$  having the smallest  $t_{\parallel}$ , and thus flattest in-plane dispersion. The strong out-of-plane nearest-neighbor hopping ( $t_{\perp}^{(s)}$ ), in turn, grows significantly in magnitude from Cl ( $-127$  meV) to Br ( $-162$  meV) and to I ( $-208$  meV), see red markers in Fig. 5a. The “weak link” in the out-of-plane directions ( $t_{\perp}^{(w)}$ ) is vanishingly small for Cl ( $-3$  meV) and only mildly grows towards I ( $-24$  meV), see blue markers in Fig. 5. This reflects the increasing bilayer hybridization between the inter-layer dimerized trimers, leading to the growth of the bonding/anti-bonding single particle splitting, as observed around  $\Gamma$  in Fig. 3. In  $\text{Nb}_3\text{F}_8^*$ , the in- and out-of-plane hoppings are of similar amplitude, such that there is no opening of a full dimerization gap throughout the Brillouin zone and only a small splitting at  $\Gamma$  is observed. To analyze the gap at the high symmetry point  $A$ , we need to take into account that there are three adjacent layer neighbors in the “weak-link” directions, such that the SSH gap of a nearest-neighbor model would be given by  $2|t_{\perp}^{(s)} - \sqrt{3}t_{\perp}^{(w)}|$ . This increases from about 243 to 332 meV going from Cl to I, indicating an increase of the dimerization strength (in  $\text{Nb}_3\text{F}_8^*$ , it is only 4 meV). The DFT gaps at  $A$  (where the SSH gap opens) are, however smaller in Br and I as compared to Cl. We understand this as a result of long-range hoppings in the out-of-plane direction, which are indeed (slightly) more pronounced in Br and I than in Cl and F.

The partially screened Coulomb interactions are dominated by density-density interactions. This is a result of having just a single molecular orbital being centered in each of the adjacent, strongly hybridized monolayers. Non-density-density interactions, such as Hund’s exchange interactions, are thus non-local, which significantly suppresses their strengths (to a few meV). Due to reduced screening in the layered vdW structures, the density-density Coulomb interactions are also non-local and show a significant long-ranged tail. The latter is visible in Fig. 5 (b) by comparing the local interactions  $U_0$  to the nearest-neighbor ones and becomes clear by comparing the full non-localities as further detailed in Appendix 1. Overall, the density-density interactions show a consistent decreasing trend from F to I. This results from two effects. First, the molecular orbital spread increases from F to I from  $4.4 \text{ \AA}^2$  to  $14.4 \text{ \AA}^2$ , which yields a decrease of the bare interactions  $v_{ijkl}$ . Simultaneously,

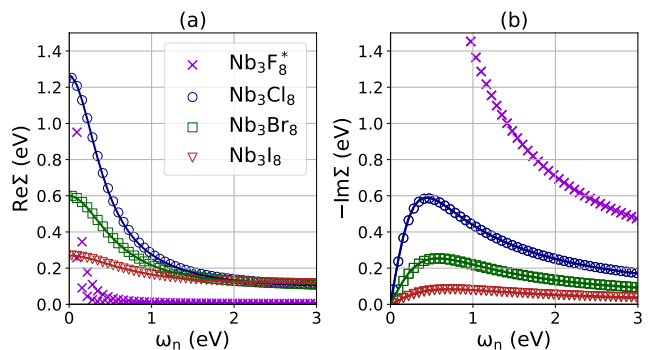


FIG. 6.  $\text{Nb}_3\text{X}_8$  Matsubara Self-Energies. (a) Real and (b) imaginary part of the self energy on Matsubara frequencies in the bonding/anti-bonding basis. Markers represent Hubbard-I results, lines represent cluster DMFT results for  $\text{Nb}_3\text{Cl}_8$ ,  $\text{Nb}_3\text{Br}_8$  &  $\text{Nb}_3\text{I}_8$ .

the effective dielectric screening  $\varepsilon$  increases from F to I, since the other bands (especially Nb  $t_{2g}^2$  and Nb  $e_g$ ) move closer to the Fermi level (see Fig. 3). Taken together, this yields the observed decrease in  $U_{ijkl}$ . In contrast to the out-of-plane hopping matrix elements, we do not see a significant bilayer hybridization effect in the non-local density-density Coulomb interactions. Comparing  $U_{1,\perp}^{(w)}$  and  $U_{1,\perp}^{(s)}$  in Fig. 5 (b) (red and blue markers), we find only small differences, which can be explained by the slightly different distances between the molecular orbital centers in these two directions.

We further see that the local Coulomb interactions  $U_0$  are very large in comparison to all hopping terms with  $U_0 \approx 2.4$  eV in  $\text{Nb}_3\text{F}_8^*$ , 1.5 eV in  $\text{Nb}_3\text{Cl}_8$ , 1.25 eV in  $\text{Nb}_3\text{Br}_8$ , and 0.8 eV in  $\text{Nb}_3\text{I}_8$ . Thus, the  $U_0/t_{\parallel}$  ratios are always larger than 80, while the  $U_0/t_{\perp}$  ratio decreases from about 12 in  $\text{Nb}_3\text{Cl}_8$  to around 4 in  $\text{Nb}_3\text{I}_8$ . These ratios point towards possible strong Coulomb-interaction induced correlation effects, which might change from system to system. To investigate this and quantify the correlation strengths, we proceed with solving the generalized Hubbard models using cluster dynamical mean-field theory.

#### D. Cluster Dynamical Mean Field Theory Self-energies at Half-Filling

Using our cRPA-based downfolded molecular-orbital models, we calculate the self-energies at half-filling within dynamical mean-field theory (DMFT) and its Hubbard-I approximation [48, 49]. Specifically, we define the impurity problem as the two inter-layer dimerized molecular (trimer) orbitals within each bilayer and include the local  $U_0$ , the strong inter-layer hybridization  $t_{\perp}^{(s)}$  as well as all inter-layer Coulomb interaction elements  $\bar{U}_{ijkl}$  (among which  $U_{\perp}^{(s)}$  is by far the largest, see Appendix 1). Accordingly, we deal with a cluster DMFT problem [19, 50, 51].

Fig. 6 shows the resulting Matsubara frequency self-energies in the diagonal  $\psi^{(\pm)}$  basis for all compounds. In this basis, the imaginary parts of the self-energy are the same for both channels ( $\text{Im}\Sigma_{(+)} = \text{Im}\Sigma_{(-)}$ ), while the real parts differ only in their signs ( $\text{Re}\Sigma_{(+)} = -\text{Re}\Sigma_{(-)}$ ) in the case of Cl, Br, and I).

The real part, as depicted in Fig. 6 (a), shows that correlation effects enhance the bonding/anti-bonding splitting, similar to the Stoner enhancement of the exchange splitting in magnetic systems. In I, the real part is almost frequency-independent, while it becomes strongly frequency-dependent moving towards Cl. This is a sign of the increasing importance of dynamic correlation effects, which necessitate (cluster) DMFT calculations. In the imaginary part depicted in Fig 6 (b), we again find a clear trend: the overall amplitudes of the self-energy gradually increase from I to Br, Cl, and F, which is a sign of the increasing degree of correlation.

Since in  $\text{Nb}_3\text{I}_8$  retardation effects are vanishingly small, while its  $\text{Re}[\Sigma(i\omega_n)] > 0$ , we can classify  $\text{Nb}_3\text{I}_8$  as a weakly correlated dimerized (or obstructed atomic) band insulator.  $\text{Nb}_3\text{Br}_8$  and  $\text{Nb}_3\text{Cl}_8$  in turn show signatures of strongly correlated insulators, while  $\text{Nb}_3\text{F}_8^*$  behaves like a conventional Mott insulator [24].

## E. Spectral functions at Integer Filling

### 1. Half-Filling ( $N_e = 2$ )

At integer filling and for large  $U_0/t_{\parallel}$ , we expect the Hubbard-I approximation [48] to be in good agreement with full cluster DMFT. This is confirmed by the self-energy results shown in Fig. 6. The Hubbard-I approximation allows us to study the systems in greater detail since it gives us direct access to retarded spectral functions without analytic continuation of Matsubara data.

The fully interacting spectral functions  $A_k(\omega)$  for all four compounds at half-filling ( $N_e = 2$  reflecting the number of electrons in the two flat bands formed by the molecular orbitals) are shown in the top row of Fig. 7. In all cases, we see that the gap is widened in comparison to the mean-field DFT solutions shown in Fig. 3. For  $\text{Nb}_3\text{Cl}_8$ ,  $\text{Nb}_3\text{Br}_8$ , and  $\text{Nb}_3\text{I}_8$ , we see additional flat features at lower and higher energies, which are merged with the main features in the case of  $\text{Nb}_3\text{F}_8^*$ .

Upon analyzing the exact diagonalization results of the generalized Hubbard dimer, which serves as the origin of the Hubbard-I self-energies (see Appendix 2 for details), we understand that, indeed, in  $\text{Nb}_3\text{F}_8^*$  a conventional Mott gap is formed.  $\text{Nb}_3\text{F}_8^*$  is thus a half-filled two-band Mott insulator, see Fig. 7 (a). In  $\text{Nb}_3\text{Cl}_8$  and  $\text{Nb}_3\text{Br}_8$ , the gap is formed between a lower Hubbard band (LHB) of the bonding orbital and the upper Hubbard band (UHB) of the anti-bonding orbital, which is further accompanied by a LHB of the anti-bonding orbital (below the LHB of the bonding orbital) and a UHB of the bonding orbital (above the UHB of the anti-bonding orbital), see

Fig. 7 (b-c). This is not in line with the conventional Mott insulator characterization, but shares strongly retarded self-energies as a common origin. As such, we classify  $\text{Nb}_3\text{Cl}_8$  and  $\text{Nb}_3\text{Br}_8$  as strongly correlated insulators. In  $\text{Nb}_3\text{I}_8$  all strong correlation (retardation) effects are significantly suppressed, such that the gap is best understood as being formed between the original bonding/anti-bonding bands, but slightly enhanced by Coulomb interactions, see Fig. 7 (d).  $\text{Nb}_3\text{I}_8$  is thus best classified as a weakly correlated band insulator. This is in qualitative agreement with the bilayer studies by Hu *et al.* [52] and Zhang *et al.* [21]. Zhang *et al.*, however, came to the conclusion that  $\text{Nb}_3\text{Br}_8$  is already a band insulator. Altogether, we again find clear trends going from  $\text{Nb}_3\text{F}_8^*$  to  $\text{Nb}_3\text{I}_8$ : the fundamental gap decreases and the energetic separation of the secondary LHB/UHB features increases, while their spectral weights vanish towards  $\text{Nb}_3\text{I}_8$ .

Experimentally, the fundamental gaps of  $\text{Nb}_3\text{X}_8$  have not yet been studied in great detail. To our knowledge, only  $\text{Nb}_3\text{Cl}_8$  has previously been studied in absorption and photoluminescence measurements indicating a gap size of about 1.1 eV [22, 33, 41], which is in good agreement with our theoretical prediction of about 1.16 eV [see Fig. 7 (b)].

With respect to the secondary LHB/UHBs, which are most prominent in  $\text{Nb}_3\text{Cl}_8$  and  $\text{Nb}_3\text{Br}_8$ , we note that they are only captured by cluster DMFT calculations. Using a single-site DMFT approximation, as we previously applied for bulk  $\text{Nb}_3\text{Cl}_8$  [23], these features are much more coherent and even above/below the primary LHB/UHBs. This underlines the importance of two-site cluster DMFT calculations for the LT structures, which take the full matrix structure of the self-energy (from the two orbitals depicted in Fig. 4) into account.

Since correlation effects are clearly visible in the spectral function, we have performed ARPES experiments on  $\text{Nb}_3\text{Br}_8$  and  $\text{Nb}_3\text{I}_8$  (see Methods V C and Appendix 8 for more details). Consistent with the literature [22, 24, 32–34], we see that the upmost occupied band consistently shows a splitting for all compounds, which is especially visible around  $\bar{\Gamma}$ , see Figs. 7 (f-m) for  $\text{Nb}_3\text{Br}_8$  and  $\text{Nb}_3\text{I}_8$ . This reflects the three-dimensional character of this band and the resulting  $k_z$  broadening in the system. By varying the photon energy, we probe different  $k_z$ -values along the  $A$ - $\Gamma$ - $A$  high-symmetry direction. Near the bulk  $\Gamma$  point ( $k_z = 0$ ), the lower band appears with greater spectral weight, while near the bulk  $A$  point ( $k_z = \pi$ ) the upper band dominates. For  $\text{Nb}_3\text{Br}_8$ , higher intensity from the  $A$ -point band is observed at  $h\nu=42$  eV [Fig. 7 (f,g)], whereas the higher intensity from the  $\Gamma$ -point band is observed at  $h\nu=50$  eV [Fig. 7 (h,i)]. At both photon energies, the two bands are broad and split approximately by 0.25 eV. For  $\text{Nb}_3\text{I}_8$ , the situation is similar, but with a slightly smaller splitting between the  $A$ -point and  $\Gamma$ -point bands. At  $h\nu=46$  eV [Fig. 7 (j,k)], we predominantly probe the  $\Gamma$  point, and states coming from the  $A$  point are weakly visible the energy distribution curve (EDC)

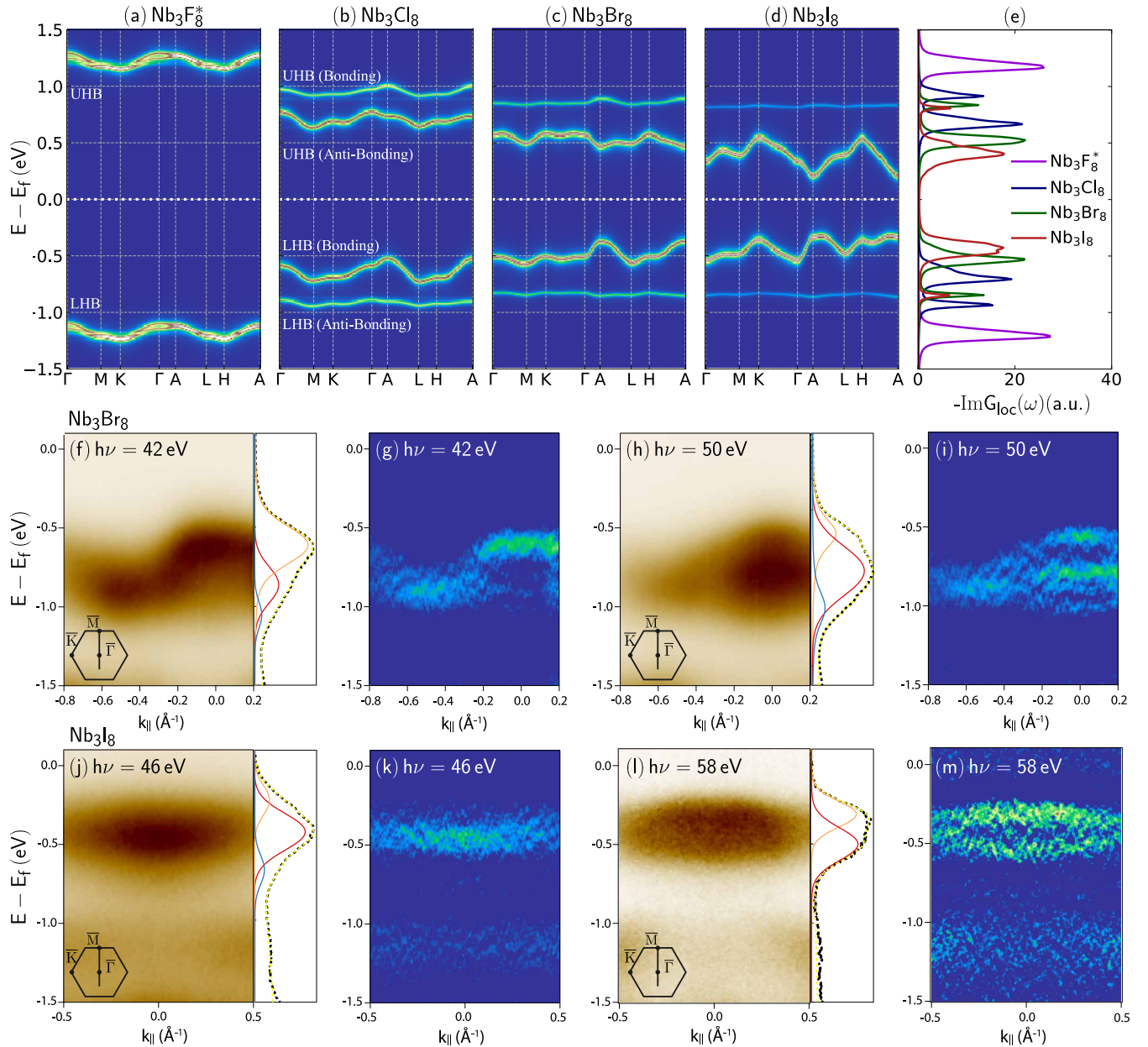


FIG. 7. **Theoretical and Experimental Spectral Functions at Half-Filling ( $N_e = 2$ ).** (a)-(d) Interacting spectral functions of  $\text{Nb}_3\text{X}_8$  within Hubbard-I approximation at half-filling. (e) Spectral function of the local Green's function. ARPES data for  $\text{Nb}_3\text{Br}_8$  obtained at photon energies of 42 eV (f-g) and 50 eV (h-i) and for  $\text{Nb}_3\text{I}_8$  at photon energies of 46 eV (j-k) and 58 eV (l-m). The left panels (f,h,j,l) show the raw ARPES data alongside EDC plots at  $k_{\parallel} = 0$ . In the EDC plots the black curve represents the raw data, the yellow dotted lines depict the overall fitting result, and the red, orange and blue lines correspond to individual fitting components. The right panels (g,i,k,m) display the 2D curvature data for the respective photon energies. In white/yellow/black colormaps white corresponds to the minimum of the signal and black to the maximum, in blue/red/green colormaps, blue corresponds to the minimum and green to the maximum.

fits, appearing 0.19 eV above the  $\Gamma$  band. In Fig. 7 (l,m), where we probe  $\text{Nb}_3\text{I}_8$  with  $h\nu=58$  eV, the  $A$ -point band becomes more intense, and the bands are again separated by 0.19 eV. This is in qualitative agreement with our calculations and the available literature.

We note that the correlation induced narrowing of the band-width in  $\Gamma$ - $A$  direction within our cluster DMFT

calculations in comparison to our DFT calculations is on the order of 30 to 50 meV and thus likely below current experimental accuracies. Also, the DFT band-width might be underestimated as a result of the applied PBE functional. Further comparison with the available ARPES results show that the lower  $t_{2g}^2$  bands, which we neglect within our cluster DMFT calculations, are still

separated from the upmost bands by about 0.5 to 1 eV (increasing from I to Br), which is in agreement with the trends expected from comparison to DFT calculations, ruling out charge-transfer insulating states.

Based on these observations it is delicate to unambiguously differentiate between conventional band, strongly correlated, and Mott insulators based on ARPES data. Recently Date *et al.* [24] suggested to analyze details of the upmost (lower Hubbard) band and its  $k_z$  dispersion to differentiate between the Mott and band insulating scenario in  $\text{Nb}_3\text{Br}_8$ . Based on our cluster DMFT calculations, we suggest to furthermore look for the existence of the secondary LHB. To this end, we analyzed our EDCs in detail, see Fig. 7 (e-h) as well as Appendix 8. We find for all photon energies that a good fit for  $\text{Nb}_3\text{Br}_8$  requires taking a third band at lower energies into account. We note that this feature might also be present in the EDC curve fits by Date *et al.* [24]. In contrast, for  $\text{Nb}_3\text{I}_8$  we do not consistently observe this third feature (as discussed in more detail in Appendix 8) and it is absent in the 58 eV data, Fig. 7 (d). This is in agreement with our cluster DMFT calculations that predict a significant spectral weight reduction of the secondary LHB in  $\text{Nb}_3\text{I}_8$  in contrast to  $\text{Nb}_3\text{Br}_8$  and is further stressed in the statistical analysis we present in Appendix 8.

## 2. Three-Quarter Filling ( $N_e = 3$ )

To uncover the degree of correlations, we further suggest studying the doping dependence of the different compounds, which could serve as a direct and unambiguous tool to differentiate between strongly and weakly correlated insulators. To this end, we start with doping the system by exactly one electron (or hole) per dimerized inter-layer trimer. Experimentally, this could be achieved by replacing one halide with one chalcogen atom per dimerized unit cell, e.g.,  $\text{Nb}_3\text{X}_{7.5}\text{Te}_{0.5}$  (note that Refs. [53] and [54] find  $\text{Nb}_3\text{Cl}_7\text{Te}$  and  $\text{Nb}_3\text{I}_7\text{Te}$  still displaying the breathing mode kagome lattice, respectively). In this case we still deal with integer filling of the two flat bands, but with  $N_e = 3$  instead of half filling with  $N_e = 2$ , such that we can still use the Hubbard-I approximation. The resulting doped spectral functions are shown in Fig. 8. From a pure band-structure perspective, we would expect that doping the systems with one electron (hole), would just half-occupy the non-interacting anti-bonding (bonding) band, making all systems good metals. Instead, we see that all systems have a gap of around 0.5 eV, which we understand as clear evidence for strong correlation effects developing in all systems, including  $\text{Nb}_3\text{I}_8$ . In detail, by doping with only one electron (hole),  $\text{Nb}_3\text{F}_8^*$  and  $\text{Nb}_3\text{Cl}_8$  are now strongly correlated charge transfer insulators (see overlap between the new uncorrelated bonding bands and the lower Hubbard band of the anti-bonding band), while  $\text{Nb}_3\text{Br}_8$  and  $\text{Nb}_3\text{I}_8$  are now Mott insulators. In all cases the gaps are opened by strong retardation effects of the self-energy

as we explain in more detail in Appendix 5. Taking the approximate particle-hole symmetry of the flat non-interacting bonding/anti-bonding bands into account, we expect that doping in the other direction, to  $N_e = 1$ , yields similar correlated electronic structures. We further note that for  $N_e = 3$ , the non-local (density-density) Coulomb interaction is playing a quantitatively important role by significantly increasing the gap. If we neglect this contribution, the strongly correlated gaps are much smaller and even close in  $\text{Nb}_3\text{F}_8^*$  (see Appendix 3).

## F. Continuous Doping ( $N_e = 2 + \delta$ )

To analyze the details of the changes from  $N_e = 2$  to  $N_e = 3$ , we performed additional calculations for the Cl, Br, and I compounds at various doping levels in between denoted by  $N_e = 2 + \delta$ . In these cases Hubbard-I is not a good approximation any more, such that we are restricted to imaginary time/frequency cluster DMFT calculations (see Methods for details). The resulting imaginary frequency self-energies are discussed in Appendix 4. In the bonding orbital channel we find for small dopings  $\delta$  stronger dynamic correlation effects in  $\text{Nb}_3\text{Cl}_8$  and  $\text{Nb}_3\text{Br}_8$  compared to  $\text{Nb}_3\text{I}_8$ , which become rather weak for all materials toward  $N_e = 3$ . The anti-bonding self-energy behaves oppositely for all systems. Upon increasing the doping from  $N_e = 2$  to  $N_e = 3$ , dynamic correlations generally increase. This is also reflected in the orbital-dependent quasiparticle weights, which we extracted from the imaginary frequency self-energies and show in Fig. 9 (a). The bonding quasiparticle weights of  $\text{Nb}_3\text{Cl}_8$  and  $\text{Nb}_3\text{Br}_8$  start close to zero in the vicinity of  $N_e = 2$ , indicative of strong correlation effects, and steadily increase with doping, while for  $\text{Nb}_3\text{I}_8$  it is larger than 0.5 at all fillings, indicative of moderate correlation effects. On the other hand, the anti-bonding orbital quasiparticle weight drastically decreases towards  $N_e = 3$  for all three compounds. This can be understood from the band perspective, where  $N_e = 3$  corresponds to a half-filled anti-bonding band. The large Coulomb interaction compared to the kinetic energy thus renders the  $N_e = 3$  systems more or less conventional single-band Mott insulators, but with a lower Hubbard band that is close to the fully-occupied bonding band.

To gain further spectroscopic insights into the continuous doping responses of the systems, we continued our imaginary frequency data to the real axis. To this end, we apply the recently proposed minimal pole representation method [55, 56] to analytically continue the matrix-valued local self-energies and calculate from this the interacting local spectra for  $\text{Nb}_3\text{Cl}_8$  and  $\text{Nb}_3\text{I}_8$ . We chose the latter two to highlight the differences between the doping dependence of a strongly and a weakly correlated system. The results are shown in Fig. 9 (b) and (c). For  $\text{Nb}_3\text{Cl}_8$  starting with a small doping of  $\delta = 0.05$ , we see that the main features shift and, importantly, a small resonance at  $\omega = 0$  eV arises, which grows in



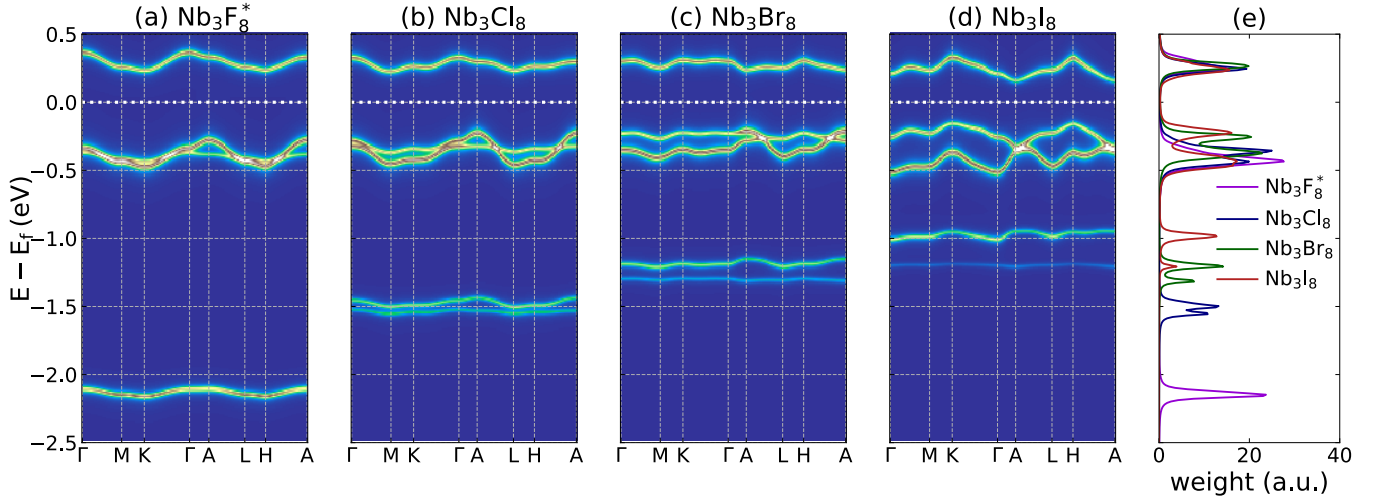


FIG. 8. **Theoretical Spectral Functions at  $N_e = 3$ .** (a-d) Interacting spectral functions of doped compounds ( $N_e = 3$ ) calculated using the Hubbard-I approximation. (e) Spectral functions of the local Green's functions.

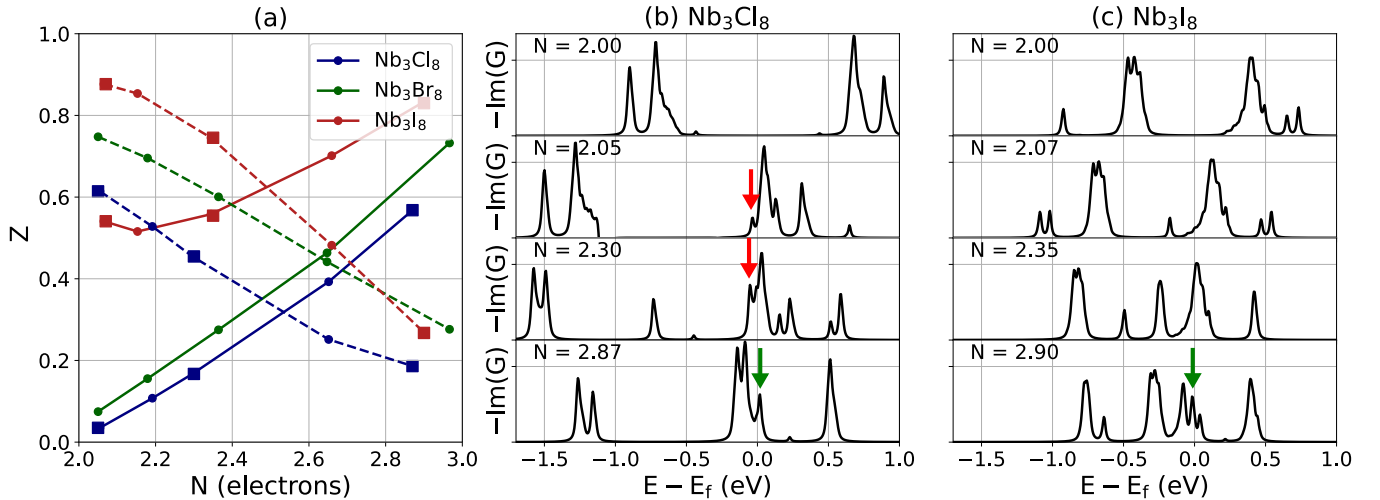


FIG. 9. **Doping Dependence.** Behavior under doping of (a) the quasiparticle weight of the bonding (solid) and anti-bonding (dashed) components and the spectral functions of (b)  $\text{Nb}_3\text{Cl}_8$  and (c)  $\text{Nb}_3\text{I}_8$ . Squares in (a) indicate doping levels, which are analysed in (b) and (c).

intensity towards  $\delta = 0.3$ , as indicated by the red arrows in Fig. 9 (b). This is reminiscent of a Kondo resonance, which is a hall-mark of doped strongly correlated insulators. Simultaneously, we see that at higher energies new resonances appear, which form at large dopings ( $\delta = 0.87$ ) a new upper Hubbard band. In fact, we can understand the  $\delta = 0.87$  data as a slightly hole-doped variant of the  $N_e = 3$  situations, which already shows the single-orbital lower and upper Hubbard bands, but here, due to finite hole doping, accompanied by a Kondo resonance, as indicated by the green arrow in Fig. 9 (b).

In contrast, the  $\text{Nb}_3\text{I}_8$  spectra more or less just shift in energy until around  $\delta = 0.35$ , without introducing any new features and especially without showing any evidence of a Kondo resonance at zero energy. This is the doping dependence we expect from conventional band in-

ulators. However, for larger dopings, we start to see new features, which are in line with our interpretation of  $\text{Nb}_3\text{I}_8$  as a single-band Mott insulator at  $N_e = 3$ . In detail, at  $\delta = 0.9$  we should understand  $\text{Nb}_3\text{I}_8$  as a hole-doped single-band Mott insulator.

### G. Quantum Magnetic Properties as the Origin of the Lattice Phase Transition

Magnetism is a ubiquitous concept in correlated materials and has correspondingly received considerable attention in  $\text{Nb}_3\text{X}_8$  as well. For the  $\text{Nb}_3\text{Cl}_8$  monolayer, our previous work [23] and recent spin-spiral DFT [26] calculations both show a magnetically ordered state with  $120^\circ$  angles between the trimer moments. For the bulk

LT phase, on the other hand, strong out-of-plane dimerization leads to singlet-formation [21, 22, 29, 35], which is common in bilayer Hubbard models at large  $U$  and large  $t_{\perp}/t_{\parallel}$  [52, 57, 58].

Although a detailed account of the quantum magnetism in  $\text{Nb}_3\text{X}_8$  is beyond the scope of this work, it is insightful to study the connection between the magnetic, electronic and lattice structure that arise from our downfolded models. Given the dominance of the Coulomb interaction over the hopping matrix elements [e.g., for  $\text{Nb}_3\text{Br}_8$   $U^{\text{eff}}$  is approximately five (hundred) times larger than the largest out-of-plane (in-plane), see Fig. 5], it is appropriate to describe the magnetic properties of  $\text{Nb}_3\text{X}_8$  using a Heisenberg model that incorporates trimer-localized magnetic moments. Accordingly, we approximate the exchange interactions as  $J_{ij} = -2(t_{ij})^2/U^{\text{eff}}$ , where  $U^{\text{eff}}$  represents the effective Coulomb interaction, which includes the renormalization of the energy cost due to non-local Coulomb interactions [23]. For more details, see Section V B. This formulation indicates that the exchange interaction is strongest when the hopping matrix element between two sites is large, leading to antiferromagnetic (AFM) exchange interactions ( $J_{ij} < 0$ ). This behavior is characteristic of materials with large  $U$ , such as all Nb halides, and explains the differences to DFT estimates that do not account for  $U$  [26, 59].

TABLE II. Molecular orbital effective exchange parameters for bulk  $\text{Nb}_3\text{X}_8$  in the LT structure in meV. The labels (s) and (w) denote strongly and weakly bound neighbors in the out-of-plane ( $\perp$ ) directions, respectively, while  $n = 1, 2, 3$  corresponds to first, second, and third nearest neighbors in the in-plane ( $\parallel$ ) direction. Note that two values of  $J_{\parallel}^{(n)}$  are provided for  $\text{Nb}_3\text{Cl}_8$  due to the slight size differences of trimers in adjacent layers, which arise from the R3 symmetry.

	$\text{Nb}_3\text{F}_8^*$	$\text{Nb}_3\text{Cl}_8$	$\text{Nb}_3\text{Br}_8$	$\text{Nb}_3\text{I}_8$
$J_{\perp}^{(s)}$	-0.20	-31.92	-62.75	-159.3
$J_{\perp}^{(w)}$	-0.09	-0.02	-0.93	-2.11
$J_{\parallel}^{(1)}$	-0.72	-0.45/-1.37	-0.13	-0.41
$J_{\parallel}^{(2)}$	-0.01	-0.05/-0.06	-0.08	-0.17
$J_{\parallel}^{(3)}$	0.00	-0.03/-0.02	-0.11	-0.36

The resulting exchange interaction parameters are listed in Table II. For the nearest-neighbor in-plane interactions  $J_{\parallel}^{(1)}$ , we do not find a clear trend from  $\text{Nb}_3\text{F}_8^*$  to  $\text{Nb}_3\text{I}_8$ . For the second- and third-nearest-neighbor in-plane interactions  $J_{\parallel}^{(2,3)}$  we, however, see a clear increasing trend from F to I. We further note that  $J_{\parallel}^{(3)}$  is (vanishingly) small in  $\text{Nb}_3\text{F}_8^*$  and  $\text{Nb}_3\text{Cl}_8$ , yet exceeds  $J_{\parallel}^{(2)}$  in  $\text{Nb}_3\text{Br}_8$  and  $\text{Nb}_3\text{I}_8$ .

Taking the bulk matrix elements as proxies for their values in the monolayer limits, we expect that all monolayers exhibit purely antiferromagnetic exchange interactions. This leads to a  $120^\circ$  Néel order in  $\text{Nb}_3\text{F}_8^*$  and

$\text{Nb}_3\text{Cl}_8$ , while  $\text{Nb}_3\text{Br}_8$  and  $\text{Nb}_3\text{I}_8$  display spin spirals with non-commensurate wave vectors, attributed to the strong exchange interactions between their third nearest neighbors as discussed in more detail in Appendix 7.

In bulk, the main difference between the LT and HT phases lies in the connectivity of the layers, as illustrated in Fig. 1 (b). In the HT phase, every trimer is connected to three trimers in the layer above and three in the layer below. Because the trimer moments within a layer are coupled antiferromagnetically, with either  $120^\circ$  or incommensurate helical order, this leads to a high degree of magnetic frustration in the HT structure: the trimer-moment cannot align consistently with all three moments in the neighboring layers. On the other hand, in the LT phase, the dimerization in the vertical direction lifts this frustration, every trimer moment has a single trimer moment to which it is coupled most strongly, and a singlet forms. The magnetic frustration in the HT phase is strongest in  $\text{Nb}_3\text{I}_8$  and gets weaker towards  $\text{Nb}_3\text{Br}_8$  and  $\text{Nb}_3\text{Cl}_8$ , as visible from the decreasing  $J_{\perp}^{(1)}$  listed in Table II. This trend clearly correlates with the decreasing critical transition temperatures. Based on this observation, we can understand the inter-layer magnetic frustration in the HT phases as a main source for the structural transition.

In Fig. 10, we further show the magnetic susceptibility of both LT and HT phases of  $\text{Nb}_3\text{Cl}_8$ , obtained from classical Monte Carlo simulations as a function of temperature and magnetic field. For computational details, please refer to Section V B. The susceptibility in the HT phase conforms to Curie-Weiss, while the structural phase transition to the LT phase has a concomitant collapse of the magnetic susceptibility. This is consistent with available experimental data [25, 29–31, 35, 40]. Very low temperatures show an upturn of the magnetic susceptibility, but we understand this as the breakdown of the classical simulation since the singlet formation can only be corrected by a full quantum mechanical treatment. Experimentally observed increases of the susceptibility at low temperatures should thus be ascribed to impurities and disorder [29, 35].

## H. Symmetry Breaking in Few-Layer Stacks and Connections to the Field Free Josephson Diode Effect

We now turn our focus to finite stacks of a few  $\text{Nb}_3\text{X}_8$  layers and their potential role for the field-free Josephson diode effect. The latter, as observed in  $\text{NbSe}_2/\text{Nb}_3\text{Br}_8/\text{NbSe}_2$  [27], requires simultaneous time-reversal (TRS) and inversion symmetry (IS) breaking [28, 60].

The IS breaking can be straightforwardly discussed:  $\text{Nb}_3\text{X}_8$  stacks with an even number of layers are inversion symmetric, while stacks with an odd number of layers break inversion symmetry. In particular, inversion symmetry is broken in the monolayer. The TRS break-

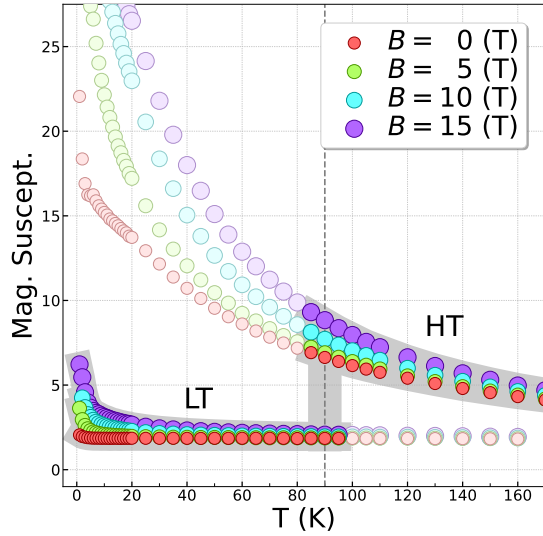
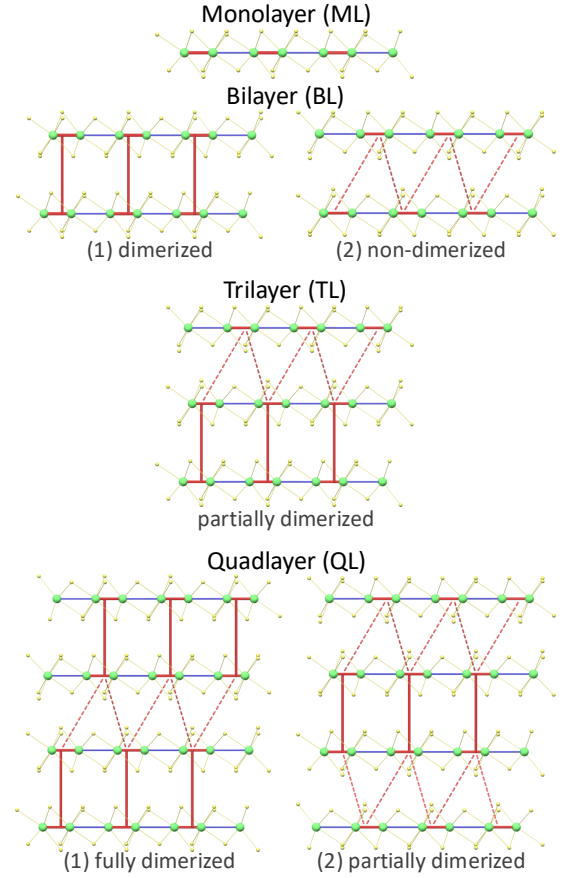


FIG. 10. **Magnetic Susceptibility of  $\text{Nb}_3\text{Cl}_8$ .** Classical Monte Carlo simulations of the magnetic susceptibility for both HT and LT structures of  $\text{Nb}_3\text{Cl}_8$  as a function of temperature  $T$  and magnetic field  $B$ . The dashed line marks the transition temperature at  $T = 90$  K.

ing requires more attention, especially with respect to the impact of the dimerization (alternating hybridization) of bilayers, which depends on the number of involved layers. Specifically, there can be top and/or bottom surface layers that only weakly hybridize with their neighbor and can therefore approximately behave like freestanding monolayers. A trilayer, for example, consists of a fully dimerized bilayer accompanied by a nearly-free monolayer, as depicted in Fig. 11. Taking the strong correlation effects into account, these surface monolayers realize (approximately) conventional single-band Mott insulators [61], which are only weakly coupled to the neighboring dimerized bilayer, as we show in more detail in Appendix 6. In contrast, mean field DFT calculations, wrongly predict the trilayer to behave like a metallic monolayer in contact with a band-insulating bilayer, cf. Appendix 6 and Ref. [28]. Thus, in the context of symmetry breakings and the Josephson diode effect, correlation properties must be considered consistently throughout the whole structure with a special focus on unpaired surface monolayers.

As previously discussed for  $\text{Nb}_3\text{Cl}_8$  [23, 26] and mentioned above and in Appendix 7, these effective monolayers likely host variants of magnetic spin-spiral states. Thus, all stacks with at least one unpaired surface layer can be classified as magnetic, which potentially breaks TRS. In contrast, stacks consisting of fully dimerized bilayers are non-magnetic as a result of the singlet formation, such that TRS stays intact.

However, whether a magnetic spin-spiral state and its potential TRS breaking also has a global effect on the electronic properties might depend on the electron coherence length [62]. If the latter is smaller than the spin-



	$\text{Nb}_3\text{F}_8^*$		$\text{Nb}_3\text{Cl}_8$		$\text{Nb}_3\text{Br}_8$		$\text{Nb}_3\text{I}_8$	
	IS	TRS	IS	TRS	IS	TRS	IS	TRS
ML	X	✓	X	✓	X	(X*)	X	(X*)
BL (1)	✓	✓	✓	✓	✓	✓	✓	✓
BL (2)	✓	✓	✓	✓	✓	(X*)	✓	(X*)
TL	X	✓	X	✓	X	(X*)	X	(X*)
QL (1)	✓	✓	✓	✓	✓	✓	✓	✓
QL (2)	✓	✓	✓	✓	✓	(X*)	✓	(X*)

FIG. 11. **Symmetries of Finite Stacks of  $\text{Nb}_3\text{X}_8$ .** Inversion (IS) and time-reversal (TRS) symmetry in monolayer (ML), bilayer (BL), trilayer (TL), and quadlayer (QL) of  $\text{Nb}_3\text{X}_8$ , taking into account various surface ("edge") terminations. The solid dark red line represents strong interlayer coupling between the nearest trimers, while the dashed line indicates weak coupling. Crosses (in brackets) indicate (possible but not necessary) symmetry-breaking. Red checkmarks denote the preservation of symmetry.

spiral wavelength, there might be a global effect. For example, the  $120^\circ$  Néel state of monolayer  $\text{Nb}_3\text{Cl}_8$  seems to leave the TRS after backfolding to the primitive unit-cell intact [26]. We find the spin-spiral wavelengths to be ranging from  $10 \text{ \AA}$  to  $18.5 \text{ \AA}$  in  $\text{Nb}_3\text{Cl}_8$  and  $\text{Nb}_3\text{I}_8$ , respectively (see Appendix 7), which is on the same order as the electronic coherence length of other Mott insulators [63–65]. Based on this, we assume a possible

global effect of the TRS breaking in the surface monolayers of  $\text{Nb}_3\text{Br}_8$  and  $\text{Nb}_3\text{I}_8$ , but possibly not in  $\text{Nb}_3\text{F}_8^*$  and  $\text{Nb}_3\text{Cl}_8$ . Additionally, we note that the interfaces to the superconducting leads in  $\text{NbSe}_2/\text{Nb}_3\text{Br}_8/\text{NbSe}_2$ , as well as magnetic impurities, might further contribute to the TRS breaking.

Taken together and as summarized in Fig. 11, this suggests that odd stacks of  $\text{Nb}_3\text{Br}_8$  and  $\text{Nb}_3\text{I}_8$  might intrinsically allow for the field-free Josephson diode effect, while  $\text{Nb}_3\text{Cl}_8$  and  $\text{Nb}_3\text{F}_8^*$  or in the case of fully dimerized bilayers in even stacks, interface effects to the encapsulating superconductors or impurities might be additionally required.

### III. CONCLUSION AND DISCUSSION

Our analysis shows that the low-energetic electronic structure as well as the magnetic properties of the whole class of  $\text{Nb}_3\text{X}_8$  are dominated by the formation of flat bands as a result of the breathing-mode kagome distortion. Since the resulting low-energetic bands are well separated from those formed by all other Nb and halides orbitals, low energy generalized Hubbard models can be straightforwardly obtained by ab initio downfolding using the constrained random phase approximation in combination with Wannier orbitals representing molecular orbitals centered at the trimerized Nb clusters.

The resulting models allow us to quantify the strengths of in- and out-of-plane hopping as well as local and non-local Coulomb matrix elements. The whole material family is in the regime of strong local interaction ( $U_0/t_{\parallel} > 80$ ). However, the ratios between these kinetic and local interaction terms suggest that from the putative  $\text{Nb}_3\text{F}_8^*$  to  $\text{Nb}_3\text{I}_8$  the degree of Coulomb correlations gradually decrease. Based on a strong coupling expansion we can further derive effective magnetic models, which show that the high-temperature crystal structures host significant inter-layer magnetic frustrations, which are lifted by singlet formation in the low-temperature structures. As these frustrations are the strongest in  $\text{Nb}_3\text{I}_8$  and gradually diminish in  $\text{Nb}_3\text{Br}_8$  and  $\text{Nb}_3\text{Cl}_8$ , the accompanying critical temperatures of the crystallographic phase transition also gradually decrease from  $\text{Nb}_3\text{I}_8$  to  $\text{Nb}_3\text{Cl}_8$ .

As a result, the low-temperature bulk materials are best understood as dimerized bilayers, which only couple weakly among each other through vdW interactions. The magnetic ground states are thus most likely singlets formed between inter-layer neighboring spins localized on the strongly hybridized molecular orbitals. On the electronic side, our combined cRPA and cluster DMFT calculations show that the halide atoms control the ratios between the local Coulomb interactions and the in- and out-of-plane hopping terms and thereby drive the bulk materials from a conventional two-band Mott insulator ( $\text{Nb}_3\text{F}_8^*$ ) to strongly correlated insulators ( $\text{Nb}_3\text{Cl}_8$  and  $\text{Nb}_3\text{Br}_8$ ) and finally to a weakly correlated band insulator

( $\text{Nb}_3\text{I}_8$ ). Thus, already in the undoped case the class of  $\text{Nb}_3\text{X}_8$  host several correlated ground states of different characters.

These correlated states can further be tuned either by doping or by the thickness of finite stacks. We showed that upon electron doping  $\text{Nb}_3\text{X}_8$  can be driven through intermediate states of correlated metals to charge transfer or conventional Mott insulators. Furthermore, as a result of the alternating strong and weak hybridization between adjacent layers, finite stacks of  $\text{Nb}_3\text{X}_8$  can host weakly hybridized surface monolayers, which host on their own already at half-filling Mott insulating states.

In terms of the in-plane trimerization, similar compounds, such as  $\text{Mo}_3\text{O}_8$ , are also accompanied by strong correlations [66], but do not allow for single molecular orbital Hubbard model descriptions. In terms of the out-of-plane dimerization,  $\text{Nb}_3\text{X}_8$  shares many similarities with bulk  $\text{VO}_2$ , one of the most well-studied correlated systems. It also hosts a crystal structure transition from a high temperature to a low temperature phase, which is accompanied by a dimerization of the vanadium atoms into pairs resulting in singlet formation [67, 68]. The latter yields a correlated gapped state, which is driven by strong Coulomb correlation effects, the dimerization, and the accompanying singlet formation [69–72], which can also be understood using a molecular orbital bonding/anti-bonding Wannier basis [73, 74]. However, the vdW material class of  $\text{Nb}_3\text{X}_8$  comes with the significant advantage of a rather simple low-energy band structure, which allows for a clean disentanglement and thus for a trustworthy downfolding to minimal correlated models.

Thus, the combination of in-plane trimerization and out-of-plane dimerization renders  $\text{Nb}_3\text{X}_8$  an extremely robust, versatile, but also simple platform to study and engineer many-body phenomena. In combination with the various and tunable degree of correlations,  $\text{Nb}_3\text{X}_8$  can thus be seen as a promising *drosophila melanogaster* of layered correlated (Mott) insulators, which offers the exciting possibility to precisely study numerous correlation phenomena both theoretically and experimentally. The models which we derived here yield an optimal theoretical framework for this purpose, and the complete model specifications for the entire  $\text{Nb}_3\text{X}_8$  family are made freely available via a public repository, see Ref. TBA.

### IV. OUTLOOK

An important difference to other prototypical bulk strongly correlated insulators is that as a result of the layered vdW structure screening is generically suppressed in  $\text{Nb}_3\text{X}_8$ , such that significantly long-ranged Coulomb interactions are present, cf. Appendix 1. These could yield a non-local coupling of holons and doublons forming Mott-excitons [75] in the strongly correlated insulators  $\text{Nb}_3\text{Br}_8$  and  $\text{Nb}_3\text{Cl}_8$  or conventional excitons in  $\text{Nb}_3\text{I}_8$ , which could be influenced by the magnetic properties of

the system. We can thus expect in-gap features in optical spectroscopy experiments, which might have been experimentally seen already in the case of  $\text{Nb}_3\text{Cl}_8$  [22, 41]. Furthermore, in few- or monolayer systems, these non-local Coulomb interactions are tunable by means of environmental screening as, e.g., resulting from substrate materials. Together with first indications that long-range Coulomb interactions in combination with doping could yield novel charge ice states [38], this renders  $\text{Nb}_3\text{X}_8$  a promising platform for strong-correlation engineering of unconventional magnetic, charge, or superconducting order but also of optical effects via non-local Coulomb interactions [76].

Another intriguing many-body engineering pathway is via chemical modification, such as already realized in admixtures of the form  $\text{Nb}_3\text{X}_{8-x}\text{Y}_x$  with X and Y being both halide atoms [22, 35]. As the halide controls the degree of correlation in this system class, such admixtures might be best understood as disordered (strongly) correlated (Mott or charge transfer) insulators. Alternatively,  $\text{Nb}_3\text{X}_{8-x}\text{Y}_x$  with Y being a chalcogen atom [53, 54] allows for precisely chemical doping to access the predicted strongly correlated metal regime and to realize the recently suggested Sordi transition [77].

Finally, the vdW nature of  $\text{Nb}_3\text{X}_8$  offers the possibility to mix and stack them into layered vdW heterostructures. Experimentally, this has already been done in the form of  $\text{NbSe}_2/\text{Nb}_3\text{Br}_8/\text{NbSe}_2$  heterostructures, which host non-reciprocal superconducting properties. Taking furthermore into account the different degrees of correlations already present within the class of  $\text{Nb}_3\text{X}_8$ , stacking them into  $\text{Nb}_3\text{X}_8/\text{Nb}_3\text{Y}_8/\text{Nb}_3\text{Z}_8$  heterostructures and/or mixing them with other correlated layered materials opens up an incredibly rich new toolbox for designing strongly correlated vdW heterostructures. So far, there is only 4Hb-TaS<sub>2</sub>, which comes with similar possibilities [78, 79]. The electronic structure of 4Hb-TaS<sub>2</sub> is, however, drastically more involved, requiring additional approximations, which are not necessary within the class of  $\text{Nb}_3\text{X}_8$ . This allows, e.g., for implementing the proposal of enhanced critical temperatures in superconducting heterostructures [80] or to realize Mott field effect transistors or correlated Schottky barriers.

Taking all these chemically, environmentally, and/or doping tunable correlation phenomena in  $\text{Nb}_3\text{X}_8$  into account renders this material class an exciting framework for many-body functionalization concepts. For these and other functionalization schemes, we however stress that the interfaces to other (substrate) materials as well as among different variants of  $\text{Nb}_3\text{X}_8$  need to be studied in detail.

## ACKNOWLEDGMENTS

The authors acknowledge useful discussions with Alberto Carta, Claude Ederer, Dmytro Afanasiev, Dieter Vollhardt, Giorgio Sangiovanni, Mikhail Titov, Maurits

Haverkort, Roser Valenti, Antoine Georges, Andrew J. Millis, and Silke Biermann. The authors especially thank Emanuel Gull and Lei Zhang for supporting the analytical continuation using Prony.

We acknowledge the National Academic Infrastructure for Supercomputing in Sweden (NAISS), partially funded by the Swedish Research Council through Grant Agreement No. 2022-06725, for awarding this project access to the LUMI supercomputer, owned by the EuroHPC Joint Undertaking and hosted by CSC IT Center for Science (Finland) and the LUMI consortium, as well as computer resources hosted by the PDC Center for High Performance Computing and the National Supercomputer Centre (Projects Nos. NAISS 2023/1-44, 2023/6-129, 2023/8-9, 2024/1-18, 2024/6-127, and 2024/8-15) where the computational pipeline was developed and tested. The material specific computations were performed at the Dutch National Supercomputer Snellius under Projects No. EINF-11321. XL acknowledges Guangzhou Elite Project scholarship (S. J. [2022] No. 1). ZD acknowledges the fellowship from the Chinese Scholarship Council (No.202206750016). MW acknowledges financial support from the Punjab Educational Endowment Fund (PEEF). AGC acknowledges the financial support of the Zernike Institute for Advanced Materials. PH acknowledges support from the Independent Research Fund Denmark (Grant No. 4258-00002B). HURS acknowledge funding from the European Research Council (ERC) under the European Union’s Horizon 2020 research and innovation programme (Grant Agreement No. 854843-FASTCORR). EGCPvL acknowledges support from the Swedish Research Council (Vetenskapsrådet, VR) under grant 2022-03090, from the Royal Physiographic Society in Lund and by eSENCE, a strategic research area for e-Science, grant number eSENCE@LU 9:1. MR acknowledges support from the Dutch Research Council (NWO) via the “TOPCORE” consortium. JA, CK, MW, MA, AGC, and MR acknowledge support from the research program “Materials for the Quantum Age” (QuMat). This program (registration number 024.005.006) is part of the Gravitation program financed by the Dutch Ministry of Education, Culture and Science (OCW).

## V. METHODS

### A. Ab Initio Modeling

We investigated the material-specific electronic structure starting from Density Functional Theory (DFT) calculations, which were carried out using the Perdew-Burke-Ernzerhof GGA exchange-correlation functional [81] within a basis of projector augmented waves [82] as implemented in the Vienna *Ab Initio* Simulation Package (VASP) [83, 84]. We applied ( $6 \times 6 \times 6$ )  $k$ -point grids in combination with a Gaussian smearing of 0.05 eV and a plane-wave cut-off of 350 eV. Pseudo-potentials from Version 5.4 of the VASP dataset



were used. The criterion for self-consistency was set to an energy change between iterations of less than  $10^{-5}$  eV.

While the experimental crystal structures of  $\text{Nb}_3\text{Cl}_8$ ,  $\text{Nb}_3\text{Br}_8$ , and  $\text{Nb}_3\text{I}_8$  are documented in the literature [29, 30, 85, 86], we determined the putative crystal structure of  $\text{Nb}_3\text{F}_8^*$  through a two-step process. In the first step we linearly interpolated the unit cell parameters and Wyckoff positions based on the experimental data for the aforementioned compounds. Recognizing that the structural parameters of these three compounds do not exhibit perfect linearity, we proceeded to a complete structural relaxation of the atomic positions in the second step, optimizing the unit cell parameters. We allowed the atomic positions to relax until the force on each atom fell below  $0.01 \text{ eV}\text{\AA}^{-1}$ . The utilized Wyckoff positions and unit cell lattice parameters are summarized in Tables IV and III, respectively.

TABLE III. In-plane ( $a$ ) and out-of-plane ( $c$ ) lattice parameters (in  $\text{\AA}$ ) for the conventional unit cell of  $\text{Nb}_3\text{X}_8$  compounds ( $\text{X} = \text{F}, \text{Cl}, \text{Br}, \text{and I}$ ) at low temperature.

	$\text{Nb}_3\text{F}_8^*$	$\text{Nb}_3\text{Cl}_8$	$\text{Nb}_3\text{Br}_8$	$\text{Nb}_3\text{I}_8$
$a$	5.7442	6.7457	7.0787	7.7000
$c$	31.1632	36.7500	40.8408	43.2400

Following the DFT calculations, we constructed maximally localized molecular orbitals  $\psi_i$  using Wannier90 [87]. Therefore we followed the same protocol as described in Ref. [23], applied here to all bulk LT structures with two layers per unit cell.

Within this basis, we calculated all single-particle (hopping) and many-body (Coulomb) matrix elements according to  $t_{ij} = \langle \psi_i | \hat{H}_{\text{DFT}} | \psi_j \rangle$  and  $U_{ijkl} = \langle \psi_i \psi_j | \hat{U}_{\text{cRPA}} | \psi_k \psi_l \rangle$ , respectively. For the latter we used the constrained Random Phase Approximation (cRPA) applying Kaltak's projector method as implemented in VASP [88]. For all systems we used a total of  $N = 256$  bands to converge the cRPA screening.

The resulting generalized Hubbard models were solved using dynamical mean-field theory calculations within TRIQS [89], applying two different impurity solvers. At integer filling and large  $U/t$ , the Hubbard-I approximation provides a reasonable description of the physics while being computationally efficient and giving access to real-frequency data directly. We use the implementation by Schüler [90]. Hubbard-I spectral functions in Figs. 7, 8, 13 & 15 were calculated at  $\beta = 5000 \text{ eV}^{-1}$  for  $\text{Nb}_3\text{F}_8^*$ ,  $1000 \text{ eV}^{-1}$  for  $\text{Nb}_3\text{Cl}_8$  and  $100 \text{ eV}^{-1}$  for  $\text{Nb}_3\text{Br}_8$  and  $\text{Nb}_3\text{I}_8$ . This ensures that the contribution to the spectrum from the first excited state, which is less and less separated in energy from  $\text{Nb}_3\text{I}_8$  to  $\text{Nb}_3\text{F}_8^*$ , is sufficiently small. The results were (Lorentzian) broadened with  $\delta = 0.01 \text{ eV}$ .

For the doped system, we use the w2dynamics solver [91] implementation of the continuous-time hy-

bridization expansion (CTHYB) [92–95] with worm sampling [96, 97]. The Discrete Lehmann Representation [98–100] is used to represent the Green's functions efficiently. The DMFT calculations were carried out at  $\beta = 100 \text{ eV}^{-1}$ .

We track the electron density  $N = \text{Tr}(\hat{\rho})$ , with  $\hat{\rho} = G(\tau = 0^-)$ , upon changes in the chemical potential. To facilitate the analysis, the self-energy and related quantities are shown in the bonding/anti-bonding basis which nearly diagonalizes the self-energy and dispersion (off-diagonal components are at least two orders of magnitude smaller than diagonal). The approximate quasiparticle weight is then derived from the self-energy on the Matsubara axis

$$Z = \left( 1 - \frac{\text{Im}[\Sigma(i\omega_n)]}{\omega_n} \Big|_{\omega_n \rightarrow 0} \right)^{-1}, \quad (2)$$

as discussed in Ref. [101].

Matsubara self-energies were analytically continued using the minimal pole representation method recently introduced by Zhang *et al.* [55, 56]. Poles were restricted to lie on the real axis. Consequently the relative strength and energy of excitations are captured, but broadening effects due to interaction are disregarded.

## B. Atomistic Spin Dynamics Simulations

To investigate the ground-state magnetic properties of the surface  $\text{Nb}_3\text{X}_8$  monolayers, as well as the temperature and magnetic field dependence of the magnetic susceptibility in bulk  $\text{Nb}_3\text{Cl}_8$ , we utilize spin dynamics simulations conducted with the SPIRIT code [102]. Our simulations are grounded in the Landau-Lifshitz-Gilbert (LLG) equation of motion to assess ground-state properties, while we employ classical Monte Carlo (MC) calculations to compute the magnetic susceptibility. Our test simulations indicate that a lattice of  $50 \times 50 \times 1$  spins is sufficient for the surface monolayer simulations (solving the LLG equations), while a  $20 \times 20 \times 4$  spins suffices for the bulk simulations (using the MC method). To minimize boundary effects, for the surface monolayer case, we consider only in-plane periodic boundary conditions, whereas for the bulk case, periodic boundaries are applied in all dimensions.

In the Monte Carlo simulations, we employed 500 thermalization steps, followed by 1,000,000 samples in the Metropolis algorithm, and conducted five decorrelation steps. The isothermal susceptibility is evaluated according to

$$\chi = \frac{1}{k_B T} (\langle \mathbf{M}^2 \rangle - \langle \mathbf{M} \rangle^2),$$

where  $\mathbf{M} = \frac{1}{N} \sum_i^N \mathbf{S}_i$  represents the average magnetization of the sample.

All simulations are based on a classical Heisenberg Hamiltonian that describes the interaction of spins  $\mathbf{S}_i$

TABLE IV. Wyckoff positions for the conventional unit cell of  $\text{Nb}_3\text{X}_8$  compounds ( $\text{X} = \text{F}, \text{Cl}, \text{Br}, \text{and I}$ ) at low temperature, characterized by the space groups  $\text{R}\bar{3}\text{m}$  and  $\text{R3}$ . The data for  $\text{Nb}_3\text{F}_8^*$  is obtained through linear interpolation from other three  $\text{Nb}_3\text{X}_8$  compounds and further structure relaxation. The layers labeled “'” and “''” represent Nb and Cl atoms located in adjacent layers of the  $\text{Nb}_3\text{X}_8$  ( $\text{R3}$ ) structure.

		$\text{Nb}_3\text{X}_8$ ( $\text{R}\bar{3}\text{m}$ )			$\text{Nb}_3\text{Cl}_8$ ( $\text{R3}$ )		
$\mathbf{r}_\alpha$	Site	$\text{Nb}_3\text{F}_8^*$	$\text{Nb}_3\text{Br}_8$	$\text{Nb}_3\text{I}_8$	Site	Layer'	Layer''
x	Nb(18h)	-0.51773	-0.53078	-0.53500	Nb(9b)	-0.52717	0.52816
y		0.51773	0.53078	0.53500		0.52717	-0.52810
z		0.08326	0.08219	0.08260		0.10784	-0.05597
x	X-1(6c)	0.33333	0.33333	0.33333	Cl-1(3a)	0.33333	-0.33333
y		-0.33333	-0.33333	-0.33333		-0.33333	0.33333
z		0.02985	0.03198	0.03127		0.05863	-0.00672
x	X-2(18h)	-0.16772	-0.16370	-0.16300	Cl-2(9b)	-0.16297	0.16573
y		0.16772	0.16370	0.16300		0.16297	-0.16553
z		0.04368	0.04534	0.04560		0.07033	-0.02027
x	X-3(6c)	-0.33333	-0.33333	-0.33333	Cl-3(3a)	-0.33333	0.33333
y		0.33333	0.33333	0.33333		0.33333	-0.33333
z		0.12504	0.11838	0.11713		0.14651	-0.09133
x	X-4(18h)	0.16466	0.16680	0.16500	Cl-4(9b)	0.16623	-0.16857
y		-0.16466	-0.16680	-0.16500		-0.16653	0.16807
z		0.12896	0.12687	0.12760		0.15167	-0.10137

located at lattice sites  $i$ :

$$H = - \sum_{i,j} J_{ij} \mathbf{S}_i \cdot \mathbf{S}_j - \sum_i \mathbf{B} \cdot \mathbf{S}_i, \quad (3)$$

where the first term represents isotropic exchange interactions and the second term accounts for the Zeeman energy in the presence of an external magnetic field  $\mathbf{B}$ . To determine the ground state properties of the monolayers, we considered a Hamiltonian without an external field and relaxed random spin configurations at zero temperature.

Given the on-site Coulomb interactions are significantly larger than the hopping matrix elements in all  $\text{Nb}_3\text{X}_8$  compounds (see Table V), we apply a strong-coupling expansion to obtain exchange interactions of the form

$$J_{\perp/\parallel} = -2(t_{\perp/\parallel})^2 / U_{\perp/\parallel}^{\text{eff}},$$

where labels  $\perp$  and  $\parallel$  denote sites  $i$  and  $j$  in the out-of-plane and in-plane directions, respectively. Instead of using  $U_0$  in the equation above, we employ  $U_{\perp}^{\text{eff}} = U_0 - U_{\perp}^{(s)}$  and  $U_{\parallel}^{\text{eff}} = U_0 - U_{\parallel}^{(1)}$  for the out-of-plane and in-plane values, respectively. This correction can be understood as the renormalization of the energy cost associated with virtual doublon-holon excitations due to non-local Coulomb interactions [103]. Such renormalization is essential for accurately capturing charge-neutral excitations; however, it is not suitable for spectral functions, which describe excitations involving changes in total charge [23, 104].

### C. ARPES Measurements

$\text{Nb}_3\text{Br}_8$  and  $\text{Nb}_3\text{I}_8$  crystals were synthesized using chemical vapor transport [27]. To avoid air exposure, crystals were mounted in a glove box and transferred to the beamline in a vacuum suitcase. Samples were cleaved *in situ* prior to ARPES measurements. The ARPES measurements were performed at the SGM3 beamline of the ASTRID2 synchrotron radiation facility at Aarhus University in Denmark [105]. Measurements were carried out at 150 K with a base pressure of  $1 \times 10^{-10}$  mbar. The ARPES data were acquired at photon energies ( $h\nu$ ) ranging from 30.5 to 130.5 eV, with energy and angular resolutions better than 50 meV and  $0.2^\circ$ , respectively. The beam spot size was  $190 \mu\text{m} \times 90 \mu\text{m}$ . The synchrotron radiation polarization and the sample-to-analyzer direction were both in the plane of incidence, and the analyzer slit was perpendicular to the plane of incidence. The EDC fitting used a linear background and Voigt profiles, employing the minimum number of fitting components required for accurate fits.

## VI. APPENDIX

### 1. Downfolded Model Parameters

In Table V we list a sub-set of the ab initio model parameters. The full parameter sets are available at TBA. We note that the Coulomb interaction has a significant

long-range tail in all compounds in both the in- and out-of-plane directions.

TABLE V. Molecular orbital Hubbard model parameters (hopping  $t_{ij}$  and density-density Coulomb matrix elements  $U_{ijjj}$ ) in units of meV for bulk  $\text{Nb}_3\text{X}_8$  in the LT structure. The lower index “0” denotes on-site values, while the upper index “(s)” and “(w)” refer to out-of-plane neighbors ( $\perp$ ) with strong and weak bonding, respectively. The upper index  $n = 1, 2, 3$  represents the first, second, and third nearest neighbors in the in-plane direction ( $\parallel$ ). Note that two values for  $U_{\parallel}^{(n)}$  and  $t_{\parallel}^{(n)}$  are provided for  $\text{Nb}_3\text{Cl}_8$  due to slight asymmetry in the size of the trimers in neighboring layers within the R3 symmetry structure.

	$\text{Nb}_3\text{F}_8^*$	$\text{Nb}_3\text{Cl}_8$	$\text{Nb}_3\text{Br}_8$	$\text{Nb}_3\text{I}_8$
$U_0$	2367.2	1498.0/1493.9	1170.9	815.5
$U_{\perp}^{(s)}$	653.7	409.8	331.7	274.8
$U_{\perp}^{(w)}$	550.4	323.5	258.0	202.6
$U_{\parallel}^{(1)}$	807.0	484.2/486.2	381.2	284.9
$U_{\parallel}^{(2)}$	523.0	288.6/288.5	234.9	185.5
$U_{\parallel}^{(3)}$	470.1	254.9/254.7	183.2	165.8
$t_0$	3319.8	4166.8/4165.5	4833.0	5471.8
$t_{\perp}^{(s)}$	-13.2	-127.0	-162.3	-207.5
$t_{\perp}^{(w)}$	-8.8	-3.1	-19.7	-23.9
$t_{\parallel}^{(1)}$	23.7	15.1/26.2	7.1	-10.4
$t_{\parallel}^{(2)}$	-2.6	5.5/4.8	5.7	6.7
$t_{\parallel}^{(3)}$	0.4	-4.8/-4.0	-6.5	-9.8

## 2. Exact Diagonalization of the Dimer Model and Relevance of Hedin Vertices

In order to establish the notion of strong and weak correlations we perform calculations using strong (Hubbard-I) and weak coupling (Hedin’s GW) approximations. Comparing the results enables us to classify the compounds in the  $\text{Nb}_3\text{X}_8$  family with respect to the degree of correlation effects.

We start this analysis by investigating the local (impurity) Green’s functions in more detail. In the Hubbard-I approximation these are equivalent to the exact diagonalization (ED) results of a generalized Hubbard dimer using the full  $U_{ijkl}$  tensor and an effective dimerization  $\tilde{t}_{\perp}$ , where  $i, j, k, l$  belong to one of the two sites representing the two molecular orbitals of the strongly hybridized/dimerized planes.

For the (simplified) Hubbard dimer with only local Coulomb interactions (i.e. only  $U_{iiii} = U$  terms taken into account), the exact interacting Green’s functions and the  $G_0W_0$  approximation can both be derived analytically [21, 106]. The latter neglects all (Hedin) vertex

contributions. The corresponding self-energies read

$$\Sigma_{ED}(\nu) = \frac{U^2}{4} \frac{1}{\nu \mp 3\tilde{t}_{\perp}} \quad (4)$$

$$\Sigma_{G_0W_0}(\omega) = \frac{U^2\tilde{t}_{\perp}}{c} \frac{1}{\nu \pm \tilde{t}_{\perp} \pm c} \quad (5)$$

with  $c = \sqrt{4\tilde{t}_{\perp}^2 + 4U\tilde{t}_{\perp}}$ . To connect this simple model to our ED calculations with the full  $U_{ijkl}$ , we fit the self-energy of the latter using the effective dimerization  $\tilde{t}_{\perp}$  as the fit parameter. We find  $\tilde{t}_{\perp} \approx 0.00, 0.15, 0.19$  and  $0.25$  eV for F, Cl, Br, and I, respectively. Setting  $U$  to the cRPA downfolded values  $U_{iiii}$ , the analytic self-energies of the simplified Hubbard dimer fit the full ED ones very well. By further comparing the Hubbard-I spectral functions obtained with and without the non-local Coulomb interactions between the two molecular orbitals of the dimer (see Appendix 3), we find that non-local Coulomb interactions do not affect the single particle Green’s functions at half-filling.

We therefore compare in Fig. 12 the spectral functions of  $G_{ED}(\omega)$  and  $G_{G_0W_0}(\omega)$  obtained for the simplified Hubbard dimer allowing us to study how relevant Hedin vertex corrections are for each system. In the case of  $\text{Nb}_3\text{Cl}_8$  we see that the ED and  $G_0W_0$  show significant discrepancies. In detail, the ED result shows a gapped local spectral function with two main peaks forming the gap, which are accompanied by two side-peaks with reduced spectral weight. We can understand these four features as lower and upper Hubbard bands from the bonding and anti-bonding orbitals, whereby the gap is formed between the lower Hubbard band of the bonding orbital and the upper Hubbard band of the anti-bonding orbital. In the  $G_0W_0$  approximation, we find a similar pole structure. However, the inner poles are at much smaller energies, while the outer poles are at much higher energies with suppressed spectral weight. Also, the nature of the  $G_0W_0$  approximation does not allow us to identify the different poles as resulting from Hubbard bands. Instead, in the  $G_0W_0$  approximation a more appropriate interpretation would be as shake-off bands resulting from charge fluctuations. Altogether, this clearly stresses the relevance of Hedin vertices for a qualitatively and quantitatively correct description of  $\text{Nb}_3\text{Cl}_8$ . This allows us to identify  $\text{Nb}_3\text{Cl}_8$  as a strongly correlated insulator. The same holds for  $\text{Nb}_3\text{Br}_8$ , albeit with smaller deviations between ED and  $G_0W_0$  results.  $\text{Nb}_3\text{F}_8^*$  in turn starts from a metallic regime and is neither quantitatively nor qualitatively well described within the  $G_0W_0$  approximation. The ED gap of  $\text{Nb}_3\text{F}_8^*$  can thus be best understood as a conventional Mott gap opened by a self-energy of the form  $\frac{U^2}{4\nu}$ . Finally, for  $\text{Nb}_3\text{I}_8$  we see that the two results are qualitatively and quantitatively very similar such that we can understand  $\text{Nb}_3\text{I}_8$  as a weakly correlated insulator, which is well approximated by the  $G_0W_0$  scheme.

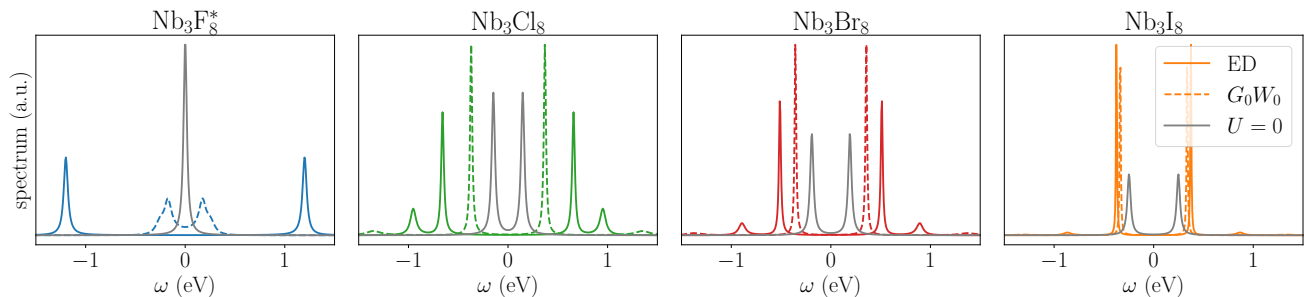


FIG. 12. Dimer model results using parameters from cRPA. We compare bare bonding/anti-bonding splitting (grey solid line) with dimer  $G_0W_0$  results (dashed lines) and exact diagonalization results (colored solid lines).

### 3. Hubbard-I Spectral Functions with only on-site Coulomb Interaction

In Fig. 13 we show the Hubbard-I spectral functions for  $N_e = 2$  and  $N_e = 3$  obtained using only local Coulomb interactions ( $U_{iii}$ ). Comparing these to Fig. 7 and Fig. 8, respectively, allows us to investigate the role of the interlayer dimer density-density Coulomb matrix elements (between the molecular orbitals  $\psi_1$  and  $\psi_2$ ) as all other elements of the full  $U_{ijkl}$  tensor were already vanishingly small.

For the undoped case ( $N_e = 2$ ), we find that the spectral functions do not change and the fundamental gaps are unaffected. This is different in the doped case ( $N_e = 3$ ). Here, removing the interlayer dimer density-density Coulomb interaction changes the spectral functions quantitatively in the case of Cl, Br, and I, and even qualitatively in the case of F. In the former cases, all gaps between sets of bands are modified when we neglect non-local Coulomb interactions. However, the qualitative properties are the same.  $Nb_3Cl_8$  and  $Nb_3Br_8$  are still charge-transfer insulators and  $Nb_3I_8$  is still a (nearly) conventional Mott insulator. In the case of  $Nb_3F_8^*$  we however find a metallic solution as soon as we neglect the non-local Coulomb interaction at  $N_e = 3$ .

### 4. Doping Dependence of DMFT Matsubara Self-Energies

Fig. 9 shows the doping-dependence of the approximate quasiparticle weights  $Z$ .  $Z$  is calculated using Eq. (2) from the imaginary part of the Matsubara self-energy shown in Fig. 14. This self-energy is calculated in cluster DMFT using `w2dynamics`.

At small doping the bonding components of the  $Nb_3Cl_8$  and  $Nb_3Br_8$  self-energies have a significant frequency dependence around zero frequency, which results in the nearly vanishing quasiparticle weight shown in Fig. 9 (a). In contrast, for  $Nb_3I_8$  these retardation effects are strongly suppressed, resulting in a significant quasiparticle weight for  $Nb_3I_8$  at small doping. This is in line

with our identifications as strongly ( $Nb_3Cl_8$  and  $Nb_3Br_8$ ) and weakly ( $Nb_3I_8$ ) correlated insulators at half-filling.

As the doping level increases towards  $N_e = 3$  we see that the frequency response of the bonding component of the self-energies is suppressed in all compounds. As a consequence, the bonding channel becomes more and more coherent with doping. In the anti-bonding component we observe a qualitatively similar behavior, i.e.  $Nb_3Cl_8$  shows the strongest retardation effects and  $Nb_3I_8$  the weakest. With increasing doping these retardation effects increase for all compounds. Thus, under (significant) electron doping even  $Nb_3I_8$  shows correlation effects in the anti-bonding channel. In fact, close to  $N_e = 3$  all systems seem to behave as hole-doped Mott insulators, which is reflected in the significantly suppressed quasiparticle weights shown in Fig. 9a.

### 5. Graphical Solution of the Dimer Models

To further clarify and visualize the qualitative differences between the strongly and weakly correlated states (with and without doping), we present in Fig. 15 the graphical solutions of the Dyson equations governing the solutions (local spectral functions) of the dimer models for all four compounds and for  $N_e = 2$  and  $N_e = 3$ , respectively. In detail, we show for all cases  $\text{Re}\Sigma(\omega)$  and  $\omega - \epsilon_{\text{loc}}$  for both, bonding and anti-bonding channels, with  $\epsilon_{\text{loc}} = \sum_{BZ} \epsilon_k$ . Therefore, the solutions to the equation

$$\omega - \epsilon_{\text{loc}} = \text{Re}[\Sigma(\omega)] \quad (6)$$

define excitation energies (poles in the spectral functions).

For  $N_e = 2$  we see three qualitatively different solutions. For  $Nb_3F_8^*$  we find (nearly) degenerate bonding and anti-bonding self-energies, both of which have a strong pole around  $\omega = 0$ . As a consequence of this (effectively) single-pole structure, we find two solutions to Eq. (6) (around  $-1.2$  and  $+1.2$  eV) yielding two features in the spectral function. This is the classic Mott-gap scenario resulting in a lower and upper Hubbard band with

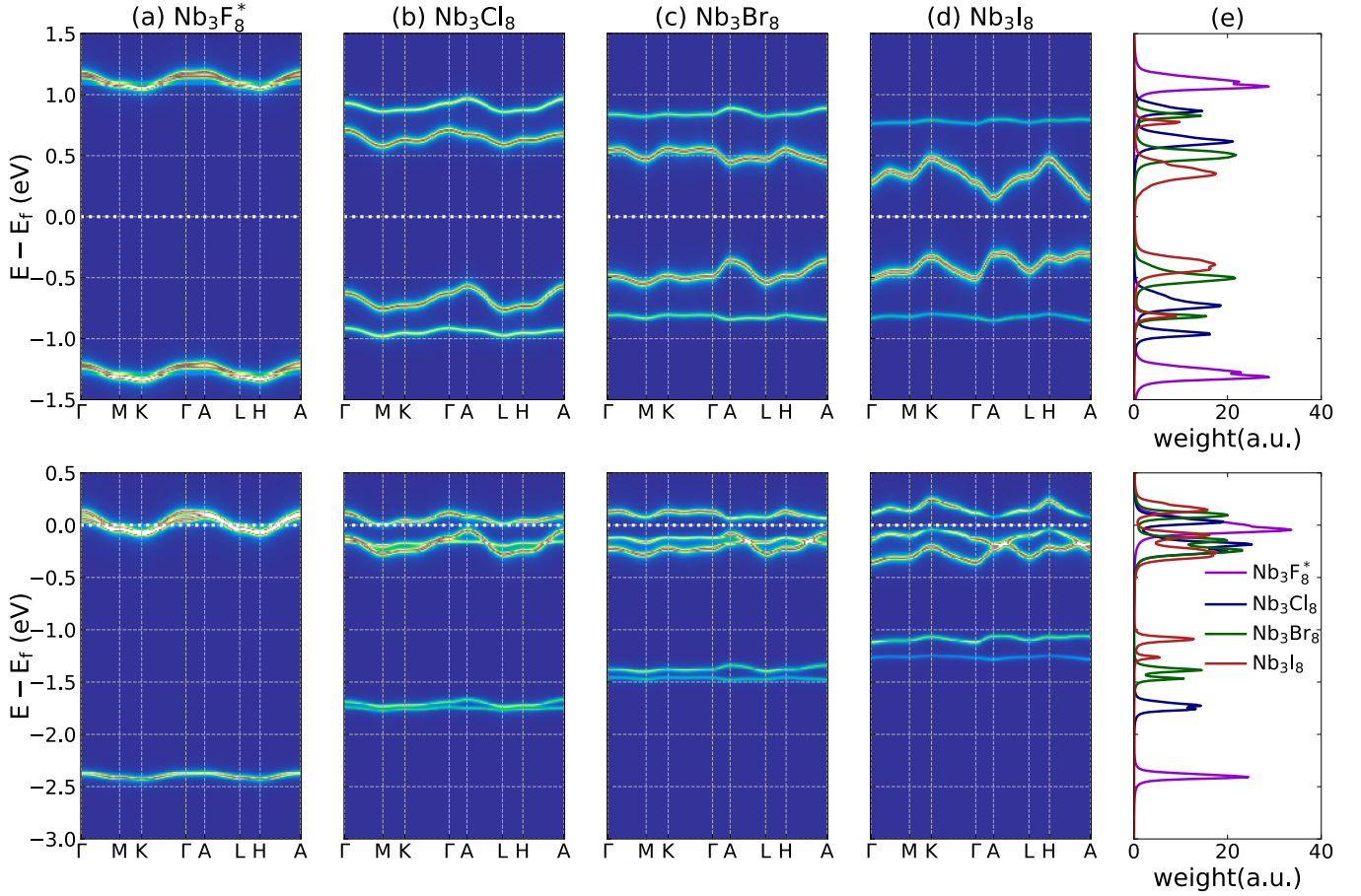


FIG. 13. (a-d) Cluster DMFT spectral functions within Hubbard-I with only on-site coulomb interactions  $U_0$  (but inter-cluster hybridization). For  $N_e = 2$  (top row) and  $N_e = 3$  (bottom row). (e) Spectral functions of the local Green's function.

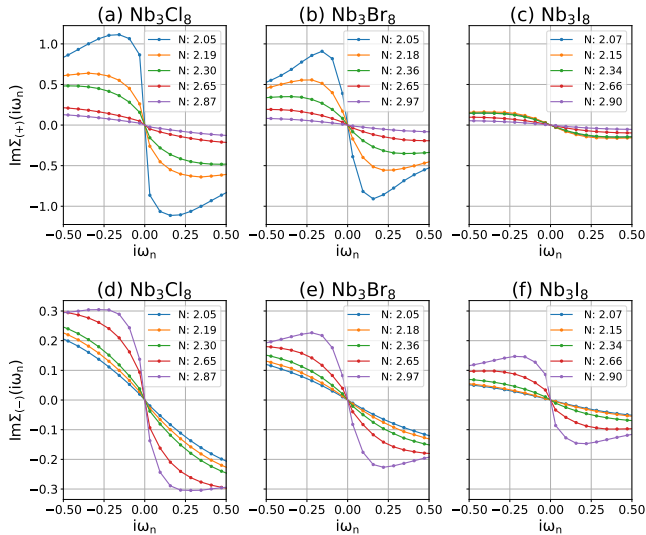


FIG. 14. Doping-dependence of the imaginary Matsubara self-energy, for the bonding (a-c) and anti-bonding component (d-f).

a gap defined by the local Coulomb interaction strength  $U$ . In contrast, for the other compounds, we see that the bonding and anti-bonding self-energies still exhibit single poles, which are, however, shifted with respect to each other. As a result we find in all cases four distinct solutions, with two main spectral features around the gap and two accompanying side features. Upon close inspection we see that the upmost occupied state is given by a solution resulting from the bonding channel, and the lowest unoccupied one by a solution resulting from the anti-bonding channel. The fundamental gap is thus always opened between the bonding and anti-bonding channel. But, due to the large  $U$  in the case of  $\text{Nb}_3\text{Cl}_8$  and  $\text{Nb}_3\text{Br}_8$  the corresponding  $\text{Re}\Sigma(\omega)$  at the solutions  $\omega = \varepsilon(\pm)$  still have a finite slope. The fundamental gaps are thus significantly affected by the Coulomb interaction and especially the retardation effects imprinted into  $\text{Re}\Sigma(\omega)$ . At a first glance, the situation seems to be similar for  $\text{Nb}_3\text{I}_8$ , but upon close inspection, we see that the gap is formed between  $\omega = \varepsilon(\pm)$  where the self-energies are nearly constant and very similar to their static values  $\text{Re}\Sigma(\omega = 0) \approx \frac{U^2}{\mp 12t_{\perp}}$  (for the bonding and anti-bonding orbital, respectively). For the reduced  $U$  and enhanced



$\tilde{t}_\perp$  of  $\text{Nb}_3\text{I}_8$ , this is dominated by  $\tilde{t}_\perp$ . The gap of  $\text{Nb}_3\text{I}_8$  is thus mostly controlled by static mean-field correlations.

In the doped case with  $N_e = 3$  the same analysis shows that the fundamental gap between highest occupied and lowest unoccupied states is always opened due to significant retardation effects, but solely in the anti-bonding channel and in (close) vicinity of a weakly correlated state resulting from the bonding orbital (see Fig. 15 right column). This single orbital Mott-insulator behavior shows a gradual increase in gap size from  $\text{Nb}_3\text{I}_8$  to  $\text{Nb}_3\text{F}^*_8$ . At  $\text{Nb}_3\text{Cl}_8$  the lower Hubbard band is so close in energy to the weakly correlated bonding-band that charge transfer occurs.

### 6. Trilayer $\text{Nb}_3\text{Br}_8$ at half-filling

In the left panel of Fig. 16 we show the Wannierized DFT band structure of a trilayer  $\text{Nb}_3\text{Br}_8$  using the molecular orbital basis and find three rather flat bands: a half-occupied metallic one surrounded by two fully occupied / empty ones. The metallic flat band results from the weakly hybridized “surface” monolayer and the other two are the bonding/anti-bonding splitted bands from the strongly hybridized bilayer. This is in line with the discussed band structure in Ref. [28]. As argued above, this mean-field picture is not properly reflecting the strong Coulomb interaction effects in the system. Therefore, we used this single-particle band structure together with the (molecular orbital) local Coulomb interaction matrix elements as obtained from our cRPA calculations (for the bulk material) to perform cluster DMFT calculations within the Hubbard-I approximation. The result is shown in the right panel of Fig. 16. We see that the Coulomb interactions induce a gap, with a set of three rather flat bands on either side of the Fermi energy. Projecting this interacting spectral function to the monolayer/bilayer basis shows that the gap is formed between bilayer states. In detail, the gap is formed, like in the bulk material, between the lower Hubbard band of the bonding orbital and the upper Hubbard band of the anti-bonding orbital. We also find a lower and upper Hubbard band of the initially metallic “surface” monolayer band.

The two systems (“surface monolayer” and bilayer) are almost completely disentangled as a result of the small hybridization between them, consistent with the interpretation of a vdW material. We expect this electronic disentanglement to be a valid picture for all finite-stacks with un-paired surface layers. We further note that in finite-stack systems the screening to the local Coulomb interactions will be a function of the  $z$ -position in the stack. The local Coulomb interaction and with it the resulting correlated gaps could thus be different in thin and thick stacks and could vary with the layer distance to the top and bottom surface.

### 7. Magnetic Order in the Surface Monolayers

While the formation of singlets in the LT bulk structures of  $\text{Nb}_3\text{Cl}_8$ ,  $\text{Nb}_3\text{Br}_8$ , and  $\text{Nb}_3\text{I}_8$  is expected, such states cannot be formed in their surface monolayers (or HT bulk structures), nor in the LT structures of  $\text{Nb}_3\text{F}_8$ . This allows us to investigate the magnetic ground state properties of the surface monolayers via a classical treatment of the effective Heisenberg Hamiltonian, see Section VB for the computational details. For the exchange interactions in the monolayer, we use  $J_\parallel^{(n)}$  values obtained for the bulk, see Table II.

Our spin dynamics simulations for all monolayers of  $\text{Nb}_3\text{X}_8$  compounds indicate that the ground state exhibits spin spirals. However, due to the finite size of the structures simulated, the resulting configurations yield commensurate spin spiral ordering. To address this issue, we analytically minimize Eq. (3) with respect to the wave vector  $\mathbf{q}$ , assuming flat spin spirals characterized by the following parametrization:

$$\mathbf{S}_i(\mathbf{q}) = \left[ \cos(\mathbf{q} \cdot \mathbf{R}_i), \sin(\mathbf{q} \cdot \mathbf{R}_i), 0 \right],$$

where  $\mathbf{R}_i$  is a position of any classical spin  $\mathbf{S}_i$ .

Fig. 17 illustrates the energy of the exchange interaction (relative to the energy of the FM state) as a function of the wave vector  $\mathbf{q}$  and the truncation distance between interacting pairs, considering up to two and three shells of nearest neighbors. The  $\text{Nb}_3\text{F}_8^*$  and  $\text{Nb}_3\text{Cl}_8$  monolayers exhibit identical propagation directions with the same value of  $|\mathbf{q}_{\min}|$ , resulting in commensurate spin spirals with a periodicity of  $1.5a$  (where  $a$  is the in-plane lattice parameter), equivalent to a  $120^\circ$ -AFM order. While the contribution from third nearest neighbors is negligible for these two compounds, the situation changes significantly for the  $\text{Nb}_3\text{Br}_8$  and  $\text{Nb}_3\text{I}_8$  monolayers. Specifically, when accounting for the third nearest neighbors in  $\text{Nb}_3\text{Br}_8$  and  $\text{Nb}_3\text{I}_8$ , the direction of spin spiral propagation is altered, and the period of modulation increases, leading to incommensurate spin configurations.

### 8. ARPES

Figs. 18 (a) and (b) show the photon energy dependent ARPES data in  $\text{Nb}_3\text{Br}_8$  and  $\text{Nb}_3\text{I}_8$ . The 2D curvature plots [107] depicted in Figs. 18 (c) and (d) reveal two dominant features which we interpret as resulting from the LHB of the bonding orbital at  $\Gamma$  and  $A$  in  $\text{Nb}_3\text{Br}_8$  and from the upmost valence band in  $\text{Nb}_3\text{I}_8$ . The significant redistribution of spectral weight in energy, as visible in Figs. 18 (a) and (b) is interpreted as the result of probing different wavevectors along  $\Gamma - A$  high-symmetry direction.

Plotting the energy peak positions and relative strength of the EDC fit [cf. Fig.7 (e-f)] vs photon energy once again reveals a third feature positioned lower in energy. This band is depicted by the dark blue dots

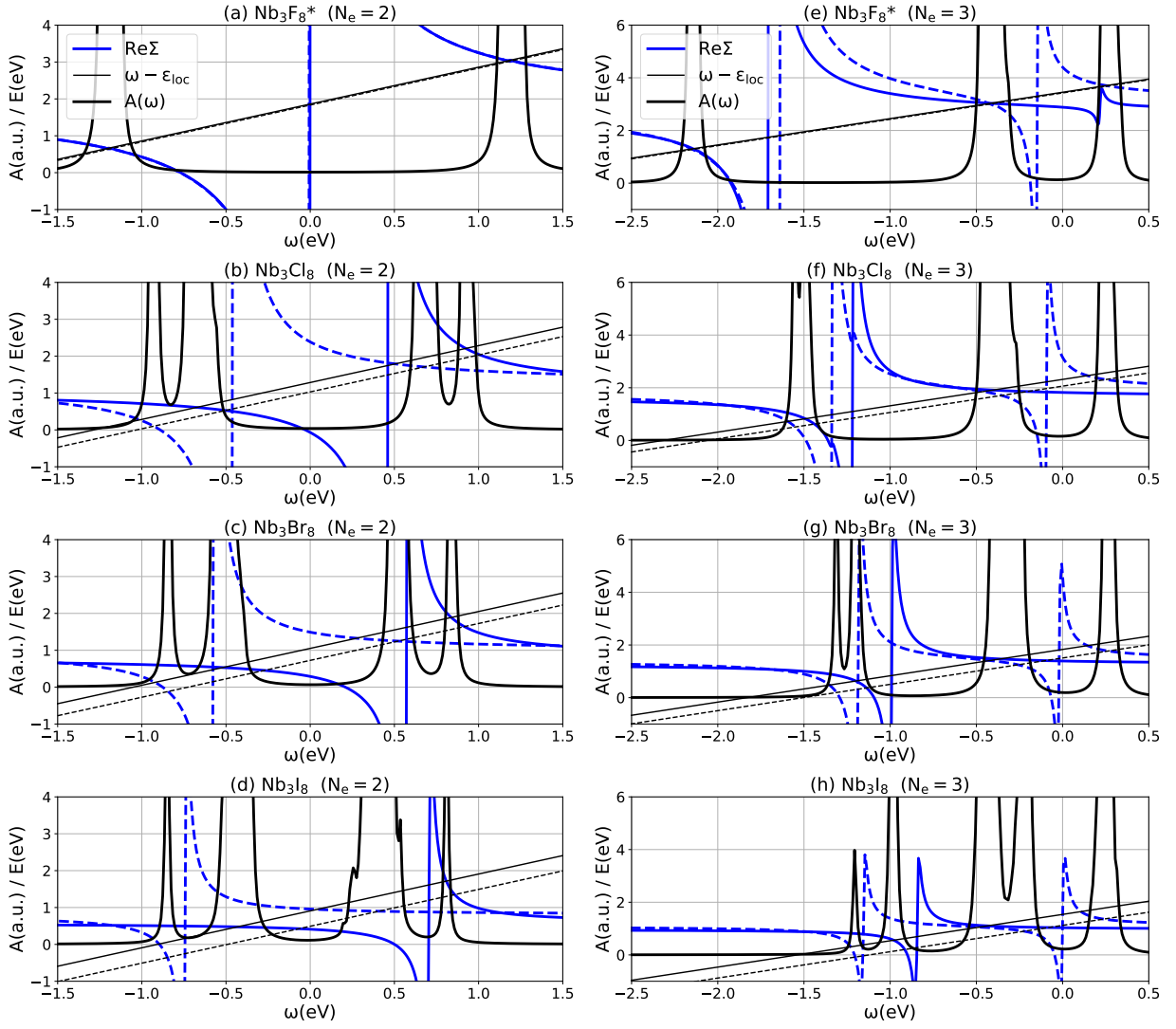


FIG. 15. Graphical representation of the local Dyson equation for the Hubbard-I calculations. Solid lines represent bonding component and dashed represent anti-bonding component. Plots in the left column (a-d) show the graphical solutions at half-filling (cf. Fig. 7). Plots in the right column (e-h) show graphical solutions at three-quarter filling:  $N_e = 3$  (cf. Fig. 8).

for  $\text{Nb}_3\text{Br}_8$  in Fig. 18 (e) and for  $\text{Nb}_3\text{I}_8$  in Fig. 18 (f). We stress that this third feature is visible in  $\text{Nb}_3\text{I}_8$  only at a few photon energies and, if so, with significantly reduced weight, as indicated by the dot sizes.

The feature is remarkably ubiquitous in the  $\text{Nb}_3\text{Br}_8$  fits and also visible in the 2D curvature plots of Fig. 18 (c). Furthermore the band has a strongly suppressed dispersion. Based on these features we interpret this as the LHB of the anti-bonding orbital. In agreement with our observations this LHB should have suppressed dispersion and reduced spectral weight in  $\text{Nb}_3\text{I}_8$  compared to  $\text{Nb}_3\text{Br}_8$  (cf. Fig.7).

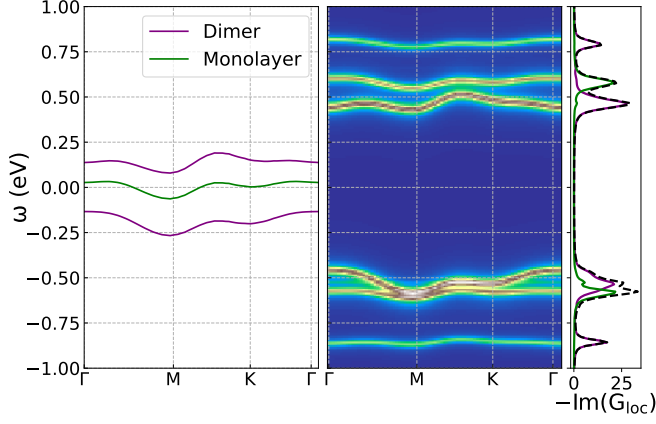


FIG. 16. Trilayer DFT and Hubbard-I results. Only on-site screened coulomb interaction are taken into account.  $U_0$  is taken from the bulk cRPA calculations.

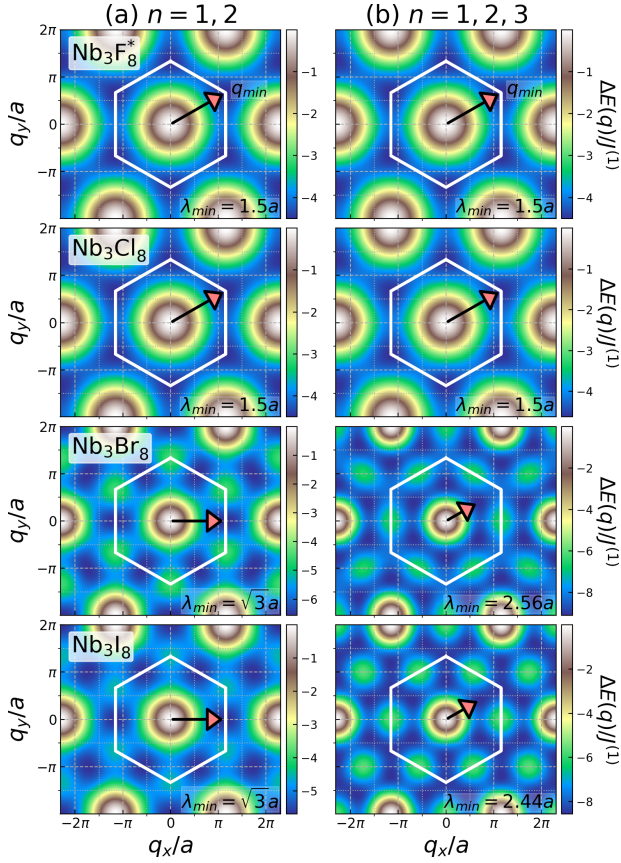


FIG. 17. Energy of the exchange interaction  $\Delta E(\mathbf{q}) = E(\mathbf{q}) - E_{\text{FM}}$  (with respect to the energy of the FM state) as a function of the spin-spiral  $\mathbf{q} = (q_x, q_y)$  vector for  $\text{Nb}_3\text{X}_8$  ML. Panels (a) and (b) illustrate the results for exchange interactions  $J_{ij}^{(n)}$  truncated to two ( $n = 1, 2$ ) and three ( $n = 1, 2, 3$ ) shells of nearest neighbors, respectively. The white hexagons represent the first Brillouin zone, while the arrows indicate the  $\mathbf{q}_{\text{min}}$  vectors corresponding to the lowest exchange interaction energy.  $\lambda_{\text{min}} = 2\pi/|\mathbf{q}|$  represents the period of the spin-spirals and  $a$  is the in-plane lattice parameter.

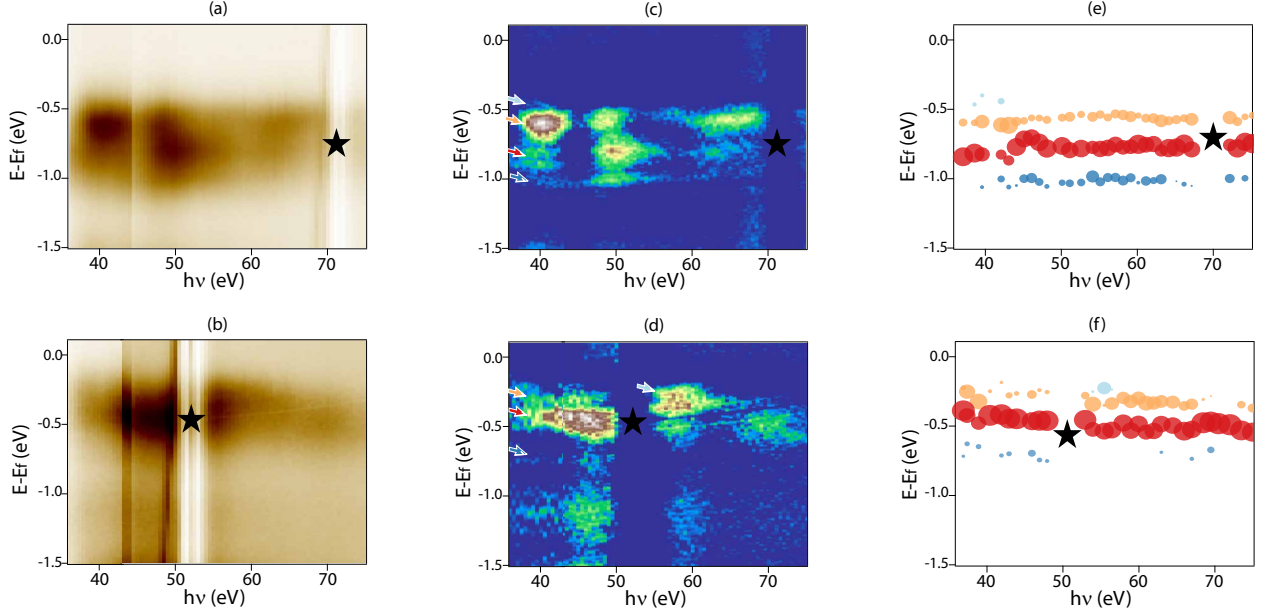


FIG. 18. Photon energy dependent angle-resolved photoemission spectroscopy data measured over a photon energy range of 36 eV to 75 eV at  $k_{\parallel} = 0$ . Fig. (a) shows the raw data for  $\text{Nb}_3\text{Br}_8$ , and (b) for  $\text{Nb}_3\text{I}_8$ . Panels (c) and (d) present the 2D curvature plots corresponding to the data in (a) and (b), respectively. The peak positions obtained from energy dispersion curve (EDC) fits for the valence band (VB) of  $\text{Nb}_3\text{Br}_8$  and  $\text{Nb}_3\text{I}_8$  are displayed in (e) and (f), respectively. Orange and red markers indicate the VB peak positions, while dark blue shows peak position of a weak band located directly below the VB. Light blue marks an additional band visible only around 38 eV for  $\text{Nb}_3\text{Br}_8$  and around 56 eV for  $\text{Nb}_3\text{I}_8$ . Regions marked with black stars indicate areas where the bands are not clearly visible due to the presence of core levels arising from higher-order excitation. In white/yellow/black colormaps white corresponds to the minimum of the signal and black to the maximum, in blue/red/green colormaps, blue corresponds to the minimum and green to the maximum.

- [1] G. Onida, L. Reining, and A. Rubio, Electronic excitations: density-functional versus many-body Green's-function approaches, *Rev. Mod. Phys.* **74**, 601 (2002).
- [2] A. Bostwick, F. Speck, K. Horn, M. Polini, R. Asgari, A. H. MacDonald, and E. Rotenberg, Observation of plasmarons in quasi-freestanding doped graphene, *Science* **328**, 999 (2010).
- [3] F. Caruso, H. Lambert, and F. Giustino, Band structures of plasmonic polarons, *Phys. Rev. Lett.* **114**, 146404 (2015).
- [4] M. Imada, A. Fujimori, and Y. Tokura, Metal-insulator transitions, *Rev. Mod. Phys.* **70**, 1039 (1998).
- [5] G. Kotliar and D. Vollhardt, Strongly correlated materials: Insights from dynamical mean-field theory, *Physics today* **57**, 53 (2004).
- [6] D. Basov, R. Averitt, and D. Hsieh, Towards properties on demand in quantum materials, *Nature materials* **16**, 1077 (2017).
- [7] A. K. Geim and I. V. Grigorieva, Van der Waals heterostructures, *Nature* **499**, 419 (2013).
- [8] K. S. Novoselov, A. K. Geim, S. V. Morozov, D. Jiang, M. I. Katsnelson, I. V. Grigorieva, S. V. Dubonos, and A. A. Firsov, Two-dimensional gas of massless Dirac fermions in graphene, *nature* **438**, 197 (2005).
- [9] J. T. Ye, Y. J. Zhang, R. Akashi, M. S. Bahramy, R. Arita, and Y. Iwasa, Superconducting dome in a gate-tuned band insulator, *Science* **338**, 1193 (2012).
- [10] A. Raja, A. Chaves, J. Yu, G. Arefe, H. M. Hill, A. F. Rigosi, T. C. Berkelbach, P. Nagler, C. Schüller, T. Korn, *et al.*, Coulomb engineering of the bandgap and excitons in two-dimensional materials, *Nature communications* **8**, 15251 (2017).
- [11] Y. Cao, V. Fatemi, A. Demir, S. Fang, S. L. Tomarken, J. Y. Luo, J. D. Sanchez-Yamagishi, K. Watanabe, T. Taniguchi, E. Kaxiras, *et al.*, Correlated insulator behaviour at half-filling in magic-angle graphene superlattices, *Nature* **556**, 80 (2018).
- [12] K. S. Burch, D. Mandrus, and J.-G. Park, Magnetism in two-dimensional van der Waals materials, *Nature* **563**, 47 (2018).
- [13] J. A. Wilson, F. Di Salvo, and S. Mahajan, Charge-density waves and superlattices in the metallic layered transition metal dichalcogenides, *Advances in Physics* **24**, 117 (1975).
- [14] X. Xi, Z. Wang, W. Zhao, J.-H. Park, K. T. Law, H. Berger, L. Forró, J. Shan, and K. F. Mak, Ising pairing in superconducting NbSe<sub>2</sub> atomic layers, *Nature Physics* **12**, 139 (2016).
- [15] Y. Cao, V. Fatemi, S. Fang, K. Watanabe, T. Taniguchi, E. Kaxiras, and P. Jarillo-Herrero, Unconventional superconductivity in magic-angle graphene superlattices, *Nature* **556**, 43 (2018).
- [16] L. Perfetti, A. Georges, S. Florens, S. Biermann, S. Mitrovic, H. Berger, Y. Tomm, H. Höchst, and M. Grioni, Spectroscopic signatures of a bandwidth-controlled Mott transition at the surface of 1T-TaSe<sub>2</sub>, *Phys. Rev. Lett.* **90**, 166401 (2003).
- [17] C. Butler, M. Yoshida, T. Hanaguri, and Y. Iwasa, Mottness versus unit-cell doubling as the driver of the insulating state in 1T-TaS<sub>2</sub>, *Nature communications* **11**, 2477 (2020).
- [18] Y. Wang, H. Wu, G. T. McCandless, J. Y. Chan, and M. N. Ali, Quantum states and intertwining phases in kagome materials, *Nature Reviews Physics* **5**, 635 (2023).
- [19] T. Maier, M. Jarrell, T. Pruschke, and M. H. Hettler, Quantum cluster theories, *Rev. Mod. Phys.* **77**, 1027 (2005).
- [20] Y. Haraguchi and K. Yoshimura, Molecular orbital electronic instability in the van der Waals kagomé semiconductor Nb<sub>3</sub>Cl<sub>8</sub>: Exploring future directions, *Journal of the Physical Society of Japan* **93**, 111002 (2024).
- [21] Y. Zhang, Y. Gu, H. Weng, K. Jiang, and J. Hu, Mottness in two-dimensional van der Waals Nb<sub>3</sub>X<sub>8</sub> monolayers (X = Cl, Br, and I), *Phys. Rev. B* **107**, 035126 (2023).
- [22] S. Gao, S. Zhang, C. Wang, S. Yan, X. Han, X. Ji, W. Tao, J. Liu, T. Wang, S. Yuan, G. Qu, Z. Chen, Y. Zhang, J. Huang, M. Pan, S. Peng, Y. Hu, H. Li, Y. Huang, H. Zhou, S. Meng, L. Yang, Z. Wang, Y. Yao, Z. Chen, M. Shi, H. Ding, H. Yang, K. Jiang, Y. Li, H. Lei, Y. Shi, H. Weng, and T. Qian, Discovery of a single-band Mott insulator in a van der Waals flat-band compound, *Phys. Rev. X* **13**, 041049 (2023).
- [23] S. Grytsiuk, M. I. Katsnelson, E. G. C. P. van Loon, and M. Rösner, Nb<sub>3</sub>Cl<sub>8</sub>: a prototypical layered Mott-Hubbard insulator, *npj Quantum Materials* **9**, 8 (2024).
- [24] M. Date, F. Petocchi, Y. Yen, J. A. Krieger, B. Pal, V. Hasse, E. C. McFarlane, C. Körner, J. Yoon, M. D. Watson, V. N. Strocov, Y. Xu, I. Kostanovski, M. N. Ali, S. Ju, N. C. Plumb, M. A. Sentef, G. Woltersdorf, M. Schüler, P. Werner, C. Felser, S. S. P. Parkin, and N. B. M. Schröter, Momentum-resolved fingerprint of Mottness in layer-dimerized Nb<sub>3</sub>Br<sub>8</sub> (2024), arXiv:2410.16199 [cond-mat.str-el].
- [25] B. Liu, Y. Zhang, X. Han, J. Sun, H. Zhou, C. Li, J. Cheng, S. Yan, H. Lei, Y. Shi, H. Yang, and S. Li, Possible quantum-spin-liquid state in van der Waals cluster magnet Nb<sub>3</sub>Cl<sub>8</sub>, *Journal of Physics: Condensed Matter* **36**, 155602 (2024).
- [26] J. Mangeri, V. R. Pavizhakumari, and T. Olsen, Magnetoelectric behavior of breathing kagomé monolayers of Nb<sub>3</sub>(Cl, Br, I)<sub>8</sub> from first-principles calculations (2024), arXiv:2411.04839 [cond-mat.mtrl-sci].
- [27] H. Wu, Y. Wang, Y. Xu, P. K. Sivakumar, C. Pasco, U. Filippozzi, S. S. Parkin, Y.-J. Zeng, T. McQueen, and M. N. Ali, The field-free Josephson diode in a van der Waals heterostructure, *Nature* **604**, 653 (2022).
- [28] Y. Zhang, Y. Gu, P. Li, J. Hu, and K. Jiang, General theory of Josephson diodes, *Physical Review X* **12**, 041013 (2022).
- [29] J. P. Sheckelton, K. W. Plumb, B. A. Trump, C. L. Broholm, and T. M. McQueen, Rearrangement of van der Waals stacking and formation of a singlet state at  $T = 90$  K in a cluster magnet, *Inorg. Chem. Front.* **4**, 481 (2017).
- [30] Y. Haraguchi, C. Michioka, M. Ishikawa, Y. Nakano, H. Yamochi, H. Ueda, and K. Yoshimura, Magnetic-nonmagnetic phase transition with interlayer charge disproportionation of Nb<sub>3</sub> trimers in the cluster compound Nb<sub>3</sub>Cl<sub>8</sub>, *Inorganic Chemistry* **56**, 3483 (2017).



- [31] D. A. Jeff, F. Gonzalez, K. Harrison, Y. Zhao, T. Fernando, S. Regmi, Z. Liu, H. R. Gutierrez, M. Neupane, J. Yang, J.-H. Chu, X. Xu, T. Cao, and S. I. Khondaker, Raman study of layered breathing kagome lattice semiconductor Nb<sub>3</sub>Cl<sub>8</sub>, *2D Materials* **10**, 045030 (2023).
- [32] S. Regmi, T. Fernando, Y. Zhao, A. P. Sakhya, G. Dhakal, I. Bin Elius, H. Vazquez, J. D. Denlinger, J. Yang, J.-H. Chu, X. Xu, T. Cao, and M. Neupane, Spectroscopic evidence of flat bands in breathing kagome semiconductor Nb<sub>3</sub>Cl<sub>8</sub>, *Communications Materials* **3**, 100 (2022).
- [33] Z. Sun, H. Zhou, C. Wang, S. Kumar, D. Geng, S. Yue, X. Han, Y. Haraguchi, K. Shimada, P. Cheng, L. Chen, Y. Shi, K. Wu, S. Meng, and B. Feng, Observation of topological flat bands in the kagome semiconductor Nb<sub>3</sub>Cl<sub>8</sub>, *Nano Letters* **22**, 4596 (2022).
- [34] S. Regmi, A. P. Sakhya, T. Fernando, Y. Zhao, D. Jeff, M. Sprague, F. Gonzalez, I. Bin Elius, M. I. Mondal, N. Valadez, D. Jarrett, A. Agosto, J. Yang, J.-H. Chu, S. I. Khondaker, X. Xu, T. Cao, and M. Neupane, Observation of flat and weakly dispersing bands in the van der Waals semiconductor Nb<sub>3</sub>Br<sub>8</sub> with breathing kagome lattice, *Phys. Rev. B* **108**, L121404 (2023).
- [35] C. M. Pasco, I. El Baggari, E. Bianco, L. F. Kourkoutis, and T. M. McQueen, Tunable magnetic transition to a singlet ground state in a 2D van der Waals layered trimerized kagomé magnet, *ACS Nano* **13**, 9457 (2019).
- [36] F. Conte, D. Ninno, and G. Cantele, Layer-dependent electronic and magnetic properties of Nb<sub>3</sub>I<sub>8</sub>, *Phys. Rev. Res.* **2**, 033001 (2020).
- [37] R. Peng, Y. Ma, X. Xu, Z. He, B. Huang, and Y. Dai, Intrinsic anomalous valley hall effect in single-layer Nb<sub>3</sub>I<sub>8</sub>, *Phys. Rev. B* **102**, 035412 (2020).
- [38] E. A. Stepanov, Signatures of a charge ice state in the doped Mott insulator Nb<sub>3</sub>Cl<sub>8</sub> (2024), arXiv:2405.19114 [cond-mat.str-el].
- [39] J.-X. Xiong, X. Zhang, and A. Zunger, Energy-lowering symmetry breaking creates a flat-band insulator in paramagnetic Nb<sub>3</sub>Cl<sub>8</sub> (2024), arXiv:2408.00145 [cond-mat.mtrl-sci].
- [40] J. Kim, Y. Lee, Y. W. Choi, T. S. Jung, S. Son, J. Kim, H. J. Choi, J.-G. Park, and J. H. Kim, Terahertz spectroscopy and DFT analysis of phonon dynamics of the layered van der Waals semiconductor Nb<sub>3</sub>X<sub>8</sub> (X = Cl, I), *ACS Omega* **8**, 14190 (2023).
- [41] Z. Meng, Z. Shi, H. Feng, H. Zhang, Z. Ren, Y. Du, F. Cheng, B. Ge, W. Cai, and W. Hao, Abnormal relaxation behavior of excited electrons in the flat band of kagome compound Nb<sub>3</sub>Cl<sub>8</sub>, *ACS Applied Materials & Interfaces* **16**, 57395 (2024).
- [42] H. Zhou, H. Liu, H. Ji, X. Li, S. Meng, and J.-T. Sun, Orbital degree of freedom induced multiple sets of second-order topological states in two-dimensional breathing kagome crystals, *npj Quantum Materials* **8**, 16 (2023).
- [43] R. Bistritzer and A. H. MacDonald, Moiré bands in twisted double-layer graphene, *Proceedings of the National Academy of Sciences* **108**, 12233 (2011).
- [44] W. P. Su, J. R. Schrieffer, and A. J. Heeger, Solitons in polyacetylene, *Phys. Rev. Lett.* **42**, 1698 (1979).
- [45] Y. Xu, L. Elcoro, Z.-D. Song, M. G. Vergniory, C. Felser, S. S. P. Parkin, N. Regnault, J. L. Mañes, and B. A. Bernevig, Filling-enforced obstructed atomic insulators, *Phys. Rev. B* **109**, 165139 (2024).
- [46] See <https://www.topologicalquantumchemistry.fr/#/detail/25767> and <https://www.topologicalquantumchemistry.fr/#/detail/421609>.
- [47] F. Aryasetiawan, M. Imada, A. Georges, G. Kotliar, S. Biermann, and A. I. Lichtenstein, Frequency-dependent local interactions and low-energy effective models from electronic structure calculations, *Phys. Rev. B* **70**, 195104 (2004).
- [48] A. I. Lichtenstein and M. I. Katsnelson, Ab initio calculations of quasiparticle band structure in correlated systems: LDA++ approach, *Phys. Rev. B* **57**, 6884 (1998).
- [49] G. Kotliar, S. Y. Savrasov, K. Haule, V. S. Oudovenko, O. Parcollet, and C. A. Marianetti, Electronic structure calculations with dynamical mean-field theory, *Rev. Mod. Phys.* **78**, 865 (2006).
- [50] A. I. Lichtenstein and M. I. Katsnelson, Antiferromagnetism and d-wave superconductivity in cuprates: A cluster dynamical mean-field theory, *Phys. Rev. B* **62**, R9283 (2000).
- [51] G. Kotliar, S. Y. Savrasov, G. Pálsson, and G. Biroli, Cellular dynamical mean field approach to strongly correlated systems, *Phys. Rev. Lett.* **87**, 186401 (2001).
- [52] C. Hu, H. Qu, X. Zhang, X.-Q. Wang, H.-Q. Lin, and G. Li, Metal-insulator transition in a correlated bilayer kagome model, *Phys. Rev. B* **110**, 235144 (2024).
- [53] H. Zhang, Z. Shi, Z. Jiang, M. Yang, J. Zhang, Z. Meng, T. Hu, F. Liu, L. Cheng, Y. Xie, J. Zhuang, H. Feng, W. Hao, D. Shen, and Y. Du, Topological flat bands in 2d breathing-kagome lattice Nb<sub>3</sub>TeCl<sub>7</sub>, *Advanced Materials* **35**, 2301790 (2023).
- [54] J. H. Yun, M. Sung, M. Choi, K. Kim, W. Yang, D. Kim, M. J. Kim, S.-H. Her, S.-Y. Choi, T.-H. Kim, J. Y. Kim, H. W. Yeom, and J. S. Kim, Flat-band electronic bipolarity in a janus and kagome van der Waals semiconductor nb<sub>3</sub>te<sub>7</sub>, *Advanced Materials* **n/a**, 2415045 (2025).
- [55] L. Zhang and E. Gull, Minimal pole representation and controlled analytic continuation of Matsubara response functions, *Phys. Rev. B* **110**, 035154 (2024).
- [56] L. Zhang, Y. Yu, and E. Gull, Minimal pole representation and analytic continuation of matrix-valued correlation functions, *Phys. Rev. B* **110**, 235131 (2024).
- [57] S. S. Kancharla and S. Okamoto, Band insulator to Mott insulator transition in a bilayer Hubbard model, *Phys. Rev. B* **75**, 193103 (2007).
- [58] H. Hafermann, M. I. Katsnelson, and A. I. Lichtenstein, Metal-insulator transition by suppression of spin fluctuations, *Europhysics Letters* **85**, 37006 (2009).
- [59] Y. Feng and Q. Yang, Enabling triferroics coupling in breathing kagome lattice Nb<sub>3</sub>X<sub>8</sub> (X = Cl, Br, I) monolayers, *J. Mater. Chem. C* **11**, 5762 (2023).
- [60] K. Misaki and N. Nagaosa, Theory of the nonreciprocal Josephson effect, *Phys. Rev. B* **103**, 245302 (2021).
- [61] In the monolayer limit, all four compounds host a single half-filled flat band around the Fermi level and, as a result of reduced screening, local Coulomb interaction matrix elements are larger than in the bulk (e.g.,  $U = 1.9$  eV for monolayer Nb<sub>3</sub>Cl<sub>8</sub> [23] versus 1.5 eV in bulk according to Table V). For a surface layer in a finite stack, the expectation is that  $U$  is between the latter values, since there is screening from one side.
- [62] Y. Wang, Y. Feng, J. G. Cheng, W. Wu, J. L. Luo, and T. F. Rosenbaum, Spiral magnetic order and pressure-induced superconductivity in transition metal compounds, *Nature Communications* **7**, 13037 (2016).

- [63] A. Pergament, Metal-insulator transition: the Mott criterion and coherence length, *Journal of Physics: Condensed Matter* **15**, 3217 (2003).
- [64] A. Kokin, Metal-dielectric phase transition in an electric field, *Fizika Tverdogo Tela* **17**, 1317 (1975).
- [65] A. Kokin, Low-frequency current fluctuations in systems with a semi-conductor to metal phase transformation, *Fizika Tverdogo Tela* **18**, 3384 (1976).
- [66] S. Nikolaev, I. Solovyev, and S. Streltsov, Quantum spin liquid and cluster Mott insulator phases in the Mo<sub>3</sub>O<sub>8</sub> magnets, *npj Quantum Materials* **6**, 25 (2021).
- [67] J. P. Pouget, H. Launois, T. M. Rice, P. Dernier, A. Gosard, G. Villeneuve, and P. Hagenmuller, Dimerization of a linear Heisenberg chain in the insulating phases of V<sub>1-x</sub>Cr<sub>x</sub>O<sub>2</sub>, *Phys. Rev. B* **10**, 1801 (1974).
- [68] S. Biermann, A. Poteryaev, A. I. Lichtenstein, and A. Georges, Dynamical singlets and correlation-assisted Peierls transition in VO<sub>2</sub>, *Phys. Rev. Lett.* **94**, 026404 (2005).
- [69] M. W. Haverkort, Z. Hu, A. Tanaka, W. Reichelt, S. V. Streltsov, M. A. Korotin, V. I. Anisimov, H. H. Hsieh, H.-J. Lin, C. T. Chen, D. I. Khomskii, and L. H. Tjeng, Orbital-assisted metal-insulator transition in VO<sub>2</sub>, *Phys. Rev. Lett.* **95**, 196404 (2005).
- [70] T. C. Koethe, Z. Hu, M. W. Haverkort, C. Schüßler-Langeheine, F. Venturini, N. B. Brookes, O. Tjernberg, W. Reichelt, H. H. Hsieh, H.-J. Lin, C. T. Chen, and L. H. Tjeng, Transfer of spectral weight and symmetry across the metal-insulator transition in VO<sub>2</sub>, *Phys. Rev. Lett.* **97**, 116402 (2006).
- [71] J. M. Tomczak and S. Biermann, Effective band structure of correlated materials: the case of VO<sub>2</sub>, *Journal of Physics: Condensed Matter* **19**, 365206 (2007).
- [72] J. M. Tomczak, F. Aryasetiawan, and S. Biermann, Effective bandstructure in the insulating phase versus strong dynamical correlations in metallic VO<sub>2</sub>, *Phys. Rev. B* **78**, 115103 (2008).
- [73] J. B. Goodenough, The two components of the crystallographic transition in VO<sub>2</sub>, *Journal of Solid State Chemistry* **3**, 490 (1971).
- [74] A. Zylbersztein and N. F. Mott, Metal-insulator transition in vanadium dioxide, *Phys. Rev. B* **11**, 4383 (1975).
- [75] N. Bittner, D. Golež, M. Eckstein, and P. Werner, Photoenhanced excitonic correlations in a Mott insulator with nonlocal interactions, *Phys. Rev. B* **101**, 085127 (2020).
- [76] E. G. C. P. van Loon, M. Schüler, D. Springer, G. Sangiovanni, J. M. Tomczak, and T. O. Wehling, Coulomb engineering of two-dimensional Mott materials, *npj 2D Materials and Applications* **7**, 47 (2023).
- [77] P.-O. Downey, O. Gingras, C.-D. Hébert, M. Charlebois, and A.-M. S. Tremblay, Doping the Mott insulating state of the triangular-lattice hubbard model reveals the sordi transition, *Phys. Rev. B* **110**, L121109 (2024).
- [78] I. Silber, S. Mathimalar, I. Mangel, A. K. Nayak, O. Green, N. Avraham, H. Beidenkopf, I. Feldman, A. Kanigel, A. Klein, M. Goldstein, A. Banerjee, E. Sela, and Y. Dagan, Two-component nematic superconductivity in 4Hb-TaS<sub>2</sub>, *Nature Communications* **15**, 824 (2024).
- [79] L. Crippa, H. Bae, P. Wunderlich, I. I. Mazin, B. Yan, G. Sangiovanni, T. Wehling, and R. Valentí, Heavy fermions vs doped Mott physics in heterogeneous Ta-dichalcogenide bilayers, *Nature Communications* **15**, 1357 (2024).
- [80] G. Mazza, A. Amaricci, and M. Capone, Interface and bulk superconductivity in superconducting heterostructures with enhanced critical temperatures, *Phys. Rev. B* **103**, 094514 (2021).
- [81] J. P. Perdew, K. Burke, and M. Ernzerhof, Generalized gradient approximation made simple, *Phys. Rev. Lett.* **77**, 3865 (1996).
- [82] P. E. Blöchl, Projector augmented-wave method, *Phys. Rev. B* **50**, 17953 (1994).
- [83] G. Kresse and J. Furthmüller, Efficient iterative schemes for ab initio total-energy calculations using a plane-wave basis set, *Phys. Rev. B* **54**, 11169 (1996).
- [84] G. Kresse and D. Joubert, From ultrasoft pseudopotentials to the projector augmented-wave method, *Phys. Rev. B* **59**, 1758 (1999).
- [85] K. Habermehl and G. Meyer, Triniobiumoctabromide, Nb<sub>3</sub>Br<sub>8</sub>, revisited, *Zeitschrift für Naturforschung B* **65**, 770 (2010).
- [86] S. Magonov, P. Zönnchen, H. Rotter, H. Cantow, G. Thiele, J. Ren, and M. Whangbo, Scanning tunneling and atomic force microscopy study of layered transition metal halides Nb<sub>3</sub>X<sub>8</sub> (X= Cl, Br, I), *Journal of the American Chemical Society* **115**, 2495 (1993).
- [87] A. A. Mostofi, J. R. Yates, Y.-S. Lee, I. Souza, D. Vanderbilt, and N. Marzari, wannier90: A tool for obtaining maximally-localised Wannier functions, *Computer Physics Communications* **178**, 685 (2008).
- [88] M. Kaltak, *Merging GW with DMFT*, Ph.D. thesis, University of Vienna (2015).
- [89] O. Parcollet, M. Ferrero, T. Ayral, H. Hafermann, I. Krivenko, L. Messio, and P. Seth, TRIQS: A toolbox for research on interacting quantum systems, *Computer Physics Communications* **196**, 398 (2015).
- [90] M. Schüler, TRIQS/hubbardI - a Hubbard-I solver based on triqs atom\_diag, (2022).
- [91] M. Wallerberger, A. Hausoel, P. Gunacker, A. Kowalski, N. Parragh, F. Goth, K. Held, and G. Sangiovanni, w2dynamics: Local one- and two-particle quantities from dynamical mean field theory, *Computer Physics Communications* **235**, 388 (2019).
- [92] P. Werner, A. Comanac, L. de' Medici, M. Troyer, and A. J. Millis, Continuous-time solver for quantum impurity models, *Phys. Rev. Lett.* **97**, 076405 (2006).
- [93] P. Werner and A. J. Millis, Hybridization expansion impurity solver: General formulation and application to Kondo lattice and two-orbital models, *Phys. Rev. B* **74**, 155107 (2006).
- [94] K. Haule, Quantum Monte Carlo impurity solver for cluster dynamical mean-field theory and electronic structure calculations with adjustable cluster base, *Phys. Rev. B* **75**, 155113 (2007).
- [95] E. Gull, A. J. Millis, A. I. Lichtenstein, A. N. Rubtsov, M. Troyer, and P. Werner, Continuous-time Monte Carlo methods for quantum impurity models, *Rev. Mod. Phys.* **83**, 349 (2011).
- [96] P. Gunacker, M. Wallerberger, E. Gull, A. Hausoel, G. Sangiovanni, and K. Held, Continuous-time quantum Monte Carlo using worm sampling, *Phys. Rev. B* **92**, 155102 (2015).
- [97] P. Gunacker, M. Wallerberger, T. Ribic, A. Hausoel, G. Sangiovanni, and K. Held, Worm-improved estimators in continuous-time quantum Monte Carlo, *Phys. Rev. B* **94**, 125153 (2016).

- [98] J. Kaye, K. Chen, and O. Parcollet, Discrete Lehmann representation of imaginary time Green's functions, *Physical Review B* **105**, 235115 (2022).
- [99] J. Kaye, K. Chen, and H. U. R. Strand, libdlr: Efficient imaginary time calculations using the discrete Lehmann representation, *Computer Physics Communications* **280**, 108458 (2022).
- [100] J. Kaye, H. U. R. Strand, and N. Wentzell, cppdlr: Imaginary time calculations using the discrete Lehmann representation, *Journal of Open Source Software* **9**, 6297 (2024).
- [101] L.-F. Arsenault, P. Sémon, and A.-M. Tremblay, Benchmark of a modified iterated perturbation theory approach on the fcc lattice at strong coupling, *Physical Review B* **86**, 085133 (2012).
- [102] G. P. Müller, M. Hoffmann, C. Dißelkamp, D. Schürhoff, S. Mavros, M. Sallermann, N. S. Kiselev, H. Jónsson, and S. Blügel, Spirit: Multifunctional framework for atomistic spin simulations, *Phys. Rev. B* **99**, 224414 (2019).
- [103] M. Schüler, M. Rösner, T. O. Wehling, A. I. Lichtenstein, and M. I. Katsnelson, Optimal Hubbard models for materials with nonlocal Coulomb interactions: Graphene, silicene, and benzene, *Phys. Rev. Lett.* **111**, 036601 (2013).
- [104] H.-K. Tang, I. Yudhistira, U. Chattopadhyay, M. Ulybyshev, P. Sengupta, F. F. Assaad, and S. Adam, Spectral functions of lattice fermions on the honeycomb lattice with Hubbard and long-range Coulomb interactions, *Phys. Rev. B* **110**, 155120 (2024).
- [105] S. Hoffmann, C. Søndergaard, C. Schultz, Z. Li, and P. Hofmann, An undulator-based spherical grating monochromator beamline for angle-resolved photoemission spectroscopy, *Nuclear Instruments and Methods in Physics Research Section A: Accelerators, Spectrometers, Detectors and Associated Equipment* **523**, 441 (2004).
- [106] J. M. Tomczak, *Propriétés spectrales et optiques des Matériaux corrélés*, Thesis, Ecole Polytechnique X (2007).
- [107] P. Zhang, P. Richard, T. Qian, Y.-M. Xu, X. Dai, and H. Ding, A precise method for visualizing dispersive features in image plots, *Review of Scientific Instruments* **82**, 043712 (2011).